Gemini NIFS survey of feeding and feedback in nearby active galaxies – IV. Excitation

Rogemar A. Riffel [ID],[1]★ Marina Bianchin,[1] Rogério Riffel [ID],[2] Thaisa Storchi-Bergmann,[2] Astor J. Schönell,[3] Luis Gabriel Dahmer-Hahn,[4] Natacha Z. Dametto[5] and Marlon R. Diniz [ID][1]

[1]*Universidade Federal de Santa Maria, Departamento de Física, Centro de Ciências Naturais e Exatas, 97105-900 Santa Maria, RS, Brazil*
[2]*Instituto de Física, Universidade Federal do Rio Grande do Sul, Av. Bento Gonçalves 9500, 91501-970 Porto Alegre, RS, Brazil*
[3]*Instituto Federal de Educação, Ciência e Tecnologia Farroupilha, BR287, km 360, 97760-000 Estrada do Chapadão, Jaguari - RS, Brazil*
[4]*Laboratório Nacional de Astrofísica. Rua dos Estados Unidos, 154, CEP 37504-364 Itajubá, MG, Brazil*
[5]*Centro de Astronomía (CITEVA), Universidad de Antofagasta, Avenida Angamos 601, Antofagasta, Chile*

ABSTRACT

The near-infrared spectra of active galactic nuclei (AGN) present emission lines of different atomic and molecular species. The mechanisms involved in the origin of these emission lines in AGN are still not fully understood. We use *J*- and *K*-band integral field spectra of six luminous ($43.1 < \log L_{\rm bol}/({\rm erg\,s^{-1}}) < 44.4$) Seyfert galaxies (NGC 788, Mrk 607, NGC 3227, NGC 3516, NGC 5506, and NGC 5899) in the local Universe ($0.0039 < z < 0.0136$) to investigate the gas excitation within the inner 100–300 pc radius of the galaxies at spatial resolutions of a few tens of parsecs. In all galaxies, the H_2 emission originates from thermal processes with excitation temperatures in the range 2400–5200 K. In the high-line ratio (HLR) region of the H_2/Brγ versus [Fe II]/Paβ diagnostic diagram, which includes 29 per cent of the spaxels, shocks are the main excitation mechanism, as indicated by the correlation between the line widths and line ratios. In the AGN region of the diagram (64 per cent of the spaxels) the H_2 emission is due to the AGN radiation. The [Fe II] emission is produced by a combination of photoionization by the AGN radiation and shocks in five galaxies and is dominated by photoionization in NGC 788. The [S IX]1.2523 μm coronal emission line is present in all galaxies, and its flux distributions are extended from 80 to 185 pc from the galaxy nuclei, except for NGC 5899, in which this line is detected only in the integrated spectrum.

Key words: galaxies: active – galaxies: ISM – galaxies: nuclei – galaxies: Seyfert.

1 INTRODUCTION

The [Fe II] and molecular hydrogen emission lines are among the most prominent spectral features in the near-infrared (near-IR) spectra of active galactic nuclei (AGN), but which excitation mechanisms are responsible for their emission in AGN are still in debate (e.g. Rodríguez-Ardila et al. 2004; Rodríguez-Ardila, Riffel & Pastoriza 2005; Riffel, Rodríguez-Ardila & Pastoriza 2006b; Dors et al. 2012; Riffel et al. 2013a, 2019; Lamperti et al. 2017). Such lines can be produced by the AGN or young stars radiation field or by shocks, as for example from supernovae explosions or interaction of a radio jet with the ambient gas.

The H_2 molecule can be excited by (i) fluorescence through absorption of soft-ultraviolet photons (912–1108 Å) in the Lyman and Werner bands, existing both in star-forming (SF) regions and surrounding AGN (Black & van Dishoeck 1987), (ii) shocks (Hollenbach & McKee 1989), e.g. the interaction of a radio jet with the interstellar medium (e.g. Riffel et al. 2006a; Riffel, Storchi-Bergmann & Riffel 2015) or from supernovae explosions (Larkin et al. 1998, and references therein), (iii) X-ray illumination by a central AGN (Draine & Woods 1990; Maloney, Hollenbach & Tielens

1996) or (iv) UV radiation in dense clouds, with densities in the range 10^4 and 10^5 cm^{-3} (Sternberg & Dalgarno 1989; Davies et al. 2003) – see also Mouri (1994) for a discussion about the origin of the H_2 emission in Seyfert and Starburst galaxies. UV fluorescence is usually regarded as a non-thermal excitation process, while shocks and X-ray/UV heating are referred to as thermal processes. Thermal and non-thermal processes produce distinct relative intensities between emission lines of H_2, which can be used to discriminate the dominant excitation mechanism. Single aperture (e.g. Reunanen, Kotilainen & Prieto 2002; Rodríguez-Ardila et al. 2004, 2005; Riffel et al. 2013a) and spatially resolved (e.g. Davies et al. 2005; Storchi-Bergmann et al. 2009; Mazzalay et al. 2013; Riffel et al. 2014a, 2020) observations of AGN suggest that thermal processes dominate the production of the nuclear H_2 emission in Seyfert galaxies. Near-IR integral field spectroscopy (IFS) provides the spatial distribution and kinematics of the emission lines, which can be used to kinematically identify signatures of shocks (e.g. increased line widths associated to a radio jet or outflow), thus making it possible to discriminate between X-rays and shocks (e.g. Riffel, Storchi-Bergmann & Nagar 2010; Riffel et al. 2015).

The [Fe II] near-IR emission lines are produced in the partially ionized gas phase and [Fe II]1.2570 μm/Paβ ratio is controlled by the ratio between the volumes of the partially to fully ionized gas (Mouri et al. 1990; Mouri, Kawara & Taniguchi 1993; Rodríguez-

Ardila et al. 2005; Riffel et al. 2008; Storchi-Bergmann et al. 2009). The partially ionized zones in the central region of galaxies originate from X-ray emission (Simpson et al. 1996) in AGN or shocks due to the interaction of radio jets and gas outflows with the ambient clouds (Forbes & Ward 1993). However, to determine whether the [Fe II] emission in AGN is due to shocks or X-ray excitation, a detailed mapping of the emission-line distributions is required, which can be done by analysing IFS data of spatially resolved outflow structures in nearby AGN or more powerful distant nuclei. Even with many works investigating the excitation processes of the H_2 and [Fe II], it is still unclear if they have a common origin or are produced by a combination of distinct mechanisms.

Some studies have used near-IR IFS to map the [Fe II] and H_2 distribution and kinematics in local Seyfert galaxies at scales from few tens to few hundreds of parsecs (e.g. Riffel et al. 2006a, 2010, 2014a, 2020; Riffel, Storchi-Bergmann & Riffel 2014b; May & Steiner 2017; Durré & Mould 2018; May et al. 2020). The results reached by these studies suggest the H_2 and [Fe II] present distinct flux distributions and kinematics, with the former more restricted to the galactic plane and the latter extending to higher latitudes above it and often presenting signatures of outflows. However, the studies above are based on single objects. A detailed study on the H_2 and [Fe II] emission is performed by Colina et al. (2015), who investigated the gas excitation structure in a sample composed of 10 luminous infrared galaxies (LIRGs), 5 Seyfert galaxies, and 7 SF galaxies, using near-IR IFS. They define new areas in the [Fe II]1.6440 μm/Brγ – $H_2$2.1218 μm/Brγ diagnostic plane – previously based on single aperture measurements (e.g. Larkin et al. 1998; Reunanen et al. 2002; Riffel et al. 2006b, 2013a), for the compact, high surface brightness regions dominated by AGN, young ionizing stars, and supernovae explosions. Although Colina et al. (2015) define typical ranges of AGN line ratios, their work is not aimed to investigate in details the excitation mechanisms of the near-IR emission lines in AGN hosts.

Besides the molecular and low ionization gas, the near-IR spectra include coronal emission lines (CLs) from highly ionization gas (with typical ionization potentials larger than 100 eV), such as [S IX]1.2523 μm, which has an ionization potential of 328.2 eV. The origin of the CLs in AGN is still not clear. These lines are usually broader than those from low ionization gas and blueshifted relative to the stellar rest frame, indicating they originate in the outflowing gas from the outer portions of the Broad Line Region (Rodríguez-Ardila et al. 2002; Müller-Sánchez et al. 2011). This is further supported by photoionization models, which suggest that the nuclear coronal emission in AGN originates in the inner edge of the dusty torus (Glidden et al. 2016) and by the fact that the luminosity of CLs is correlated with the X-ray luminosity (Rodríguez-Ardila et al. 2011). However, photoionization models cannot reproduce the extended coronal gas emission on scales of a few hundred of parsecs, where the CLs originate from shocks due to the interaction of a radio jet or outflows with the interstellar medium (e.g. Rodríguez-Ardila & Fonseca-Faria 2020).

In this study, we use near-IR IFS of a sample of six luminous Seyfert galaxies (NGC 788, Mrk 607, NGC 3227, NGC 3516, NGC 5506, and NGC 5899) to investigate the origin of the [Fe II] and H_2 emission on scales of ~100 pc and map the spatial extent of the coronal emission lines. We use the same sample previously discussed in Schönell et al. (2019), where we present the data, emission-line flux, surface gas mass distributions and kinematic maps. There, we found that H_2 emission originates mostly from gas rotating in the galaxy plane, while the ionized gas shows signatures of outflows. In addition, the amount of gas available in the inner kpc of these galaxies is, at least, 100 times larger than needed to power the central AGN. This paper is organized as follows. Section 2 presents information about the sample, data reduction, and measurements, Section 3 presents the emission-line flux distributions and emission-line ratio diagnostic diagrams, while the discussion is presented in Section 4 and our conclusions in Section 5. We use a $h = 0.7$, $\Omega_m = 0.3$, and $\Omega_\Lambda = 0.7$ cosmology throughout this paper.

2 THE SAMPLE, DATA, AND MEASUREMENTS

Our sample is composed of six nearby and luminous Seyfert galaxies. They are part of a sample of 29 galaxies from the Gemini NIFS survey of feeding and feedback processes in nearby active galaxies (Riffel et al. 2018). The objects on the sample were selected based on the following criteria: hard X-ray (14–195 keV) luminosities $L_X \geq 10^{41.5}$ erg s^{-1}, redshifts $z \leq 0.015$ and extended [O III] emission previously reported in the literature. Nine galaxies from this sample have not yet been observed, mainly due to failures in the ALTtitude conjugate Adaptive optics for the InfraRed (ALTAIR) system. Among the already observed galaxies in both J and K bands using adaptive optics, we select for this study the six objects with no previous detailed analysis on the gas excitation: NGC 788, Mrk 607, NGC 3227, NGC 3516, NGC 5506, and NGC 5899. The six galaxies studied here are the same previously studied in Schönell et al. (2019), where we focused on the presentation of data, flux, and gas mass distribution. They are among the 50 per cent more luminous objects of the Riffel et al. (2018) sample. The galaxies of our sample have $42.36 \leq \log L_X/\mathrm{erg\,s}^{-1} \leq 43.51$ (Oh et al. 2018) – which corresponds to bolometric luminosities in the range $43.44 \leq \log L_{bol}/\mathrm{erg\,s}^{-1} \leq 44.83$, using the relation between L_X and L_{bol} presented in Ichikawa et al. (2017) – and redshifts in the range $0.004 \leq z \leq 0.014$ (corresponding to 17–60 Mpc).

The J- and K-band observations were performed with the Gemini Near-infrared Integral Field Spectrograph (NIFS, McGregor et al. 2003), which has a field of view of 3×3 arcsec^2 and angular sampling of 0.103×0.042 arcsec^2. NIFS was coupled to the ALTAIR system and the resulting angular resolutions are in the range 0.12–0.18 arcsec, corresponding to a few tens of parsecs.

We follow the standard procedure to reduce the raw data using the GEMINI IRAF package, including the trimming of the images, flat-fielding, cosmic-ray rejection, sky subtraction, wavelength, and s-distortion calibrations, removal of the telluric features, flux calibration and construction of the datacubes for each individual exposure on each science target at an angular sampling of 0.05×0.05 arcsec^2. The final datacubes are obtained by median combining the individual datacubes in each band using the peak of the continuum emission as reference. More details about the sample, instrument, observations, and data reduction are presented in previous papers (Riffel et al. 2017, 2018; Schönell et al. 2019).

To investigate the origin of hot molecular and ionized gas emission in the galaxies of our sample, we measure the emission-line flux distribution by adopting the following procedure: first, we follow Liu et al. (2013) and fit each emission line by a combination of three Gaussian functions using the IFSCUBE code (Ruschel-Dutra 2020). The choice of the number of components has no physical motivation and simply aims to reproduce the observed profiles. In previous papers by our group, we used the PROFIT code (Riffel 2010) to fit the emission-line profiles by Gaussian or Gauss–Hermite profiles (e.g. Schönell et al. 2019). The IFSCUBE code is more suitable for this work as it perform the fits of the emission lines in each band simultaneously and allow the inclusion of more than one Gaussian component or Gauss–Hermite series. The underlying continuum is represented by a third-order polynomial function. Initial guesses for
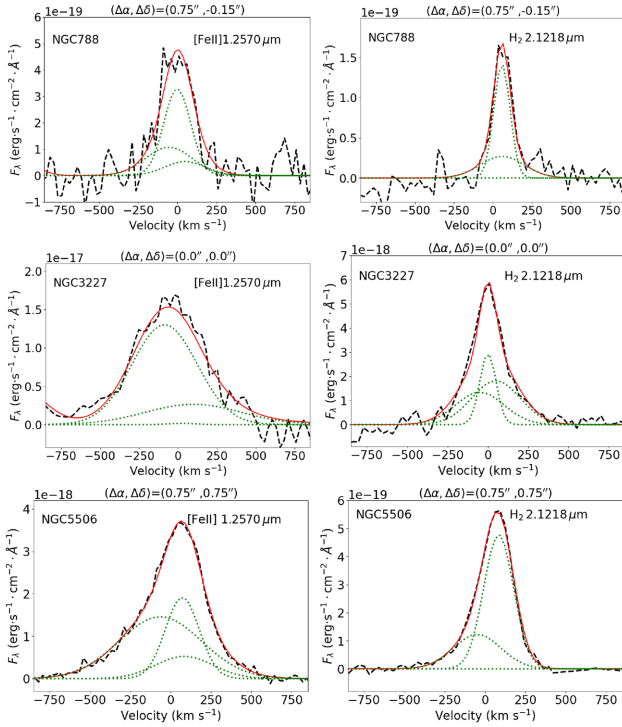
Figure 1. Examples of fits of the [Fe II]1.2570 μm (left-hand panel) and H$_2$ 2.1218 μm (right-hand panel) emission-line profiles. The continuum-subtracted observed profiles are shown as dashed black lines, the model as continuous red lines and the individual Gaussian components as dotted green lines. The galaxy name is identified in the top left-hand corner and the spaxel coordinates are shown in the title of each panel.

the centroid velocity and velocity dispersion of each component are provided to the code as obtained from the fit of the nuclear spaxel using the IRAF.SPLOT task. These guesses are used by the code to model the nuclear spaxel and then it performs the fitting of the neighbouring spaxles following a spiral loop and using the parameters from spaxels located at distances smaller than 0.25 arcsec from the fitted spaxel. Although we allow up to three Gaussian components to fit each line profile, if fewer components are able to properly reproduce the observed profile, the code fits only the number of components necessary to reproduce the observed profile, by setting the amplitudes of the unnecessary Gaussian functions as zero. Three galaxies of our sample (NGC 3227, NGC 3516, and NGC 5506) host type 1 AGN. To fit the Paβ and Brγ line profiles of these galaxies, we included an additional Gaussian to account for the Broad Line Region (BLR) emission. In Fig. 1, we show examples of the fits of the [Fe II]1.2570 μm (left-hand panel) and H$_2$ 2.1218 μm (right-hand panel) profiles for NGC 788, NGC 3227, and NGC 5506.

We integrate the fluxes in the modelled spectra within a spectral window of 1500 km s^{-1} width centred at each emission line, after the subtraction of the contribution of the continuum emission. This procedure produces flux distributions very similar to those obtained from direct integration of the observed line profiles, but the modelled spectra is less sensitive to spurious features and thus the resulting flux maps from the modelled spectra are less affected by them. For the type 1 AGN, the BLR components are subtracted from the observed spectra before the computation of the fluxes of the narrow components.

3 RESULTS

3.1 Emission-line flux distributions

The first and second rows of Figs 2–7 present the *K*-band continuum image, H$_2$ 2.1218 μm, [Fe II]1.2570 μm, [P II]1.1886 μm, Paβ and [S IX]1.2523 μm emission-line flux distributions of the galaxies of our sample. Although the H$_2$, [Fe II] and Paβ flux distributions were already shown in Schönell et al. (2019), the measurement method is distinct here, and the figures allow a comparison among the distinct emission-line flux distribution for the different galaxies. In all maps, grey regions correspond to masked locations where the line is not detected at 3σ level of the continuum noise. The dashed lines overlaid to all maps correspond to the orientation of line of nodes of the galaxy, as derived from the fitting of the stellar velocity fields by Riffel et al. (2017). The green continuous line shown in the Paβ map shows the orientation of the most collimated Paβ emission (which can be used as an indicator of the AGN ionization axis), computed using the CV2.MOMENTS python package. We performed Monte Carlo simulations with 100 iterations each, by adding random noise with amplitude of the 20th percentile flux value of the corresponding Paβ map and use the average value of the position angle of all simulations.

As already noticed by Schönell et al. (2019), distinct flux distributions are observed for the molecular and low ionized gas emission lines in most galaxies. The only exception is Mrk 607, for which both molecular and low ionization gas emission is observed mainly along the galaxy's major axis. We detect the [S IX]1.2523 μm emission in five galaxies of our sample. The [S IX] flux distribution extends to distances ≳100 pc from the nucleus for NGC 788, Mrk 607, NGC 3227, and NGC 5506, is marginally resolved for NGC 3516 and is not detected in individual spaxels for NGC 5899.

3.2 Emission-line ratio diagnostic diagrams

A way to investigate the excitation mechanisms of the near-IR emission lines is by constructing line-ratio diagrams (e.g Reunanen et al. 2002; Rodríguez-Ardila et al. 2004, 2005; Riffel et al. 2013a, 2020). The [Fe II]1.2570 μm/Paβ versus H$_2$ 2.1218 μm/Brγ is the most commonly used diagram for this purpose. We present this diagram for the individual spaxels of the galaxies of our sample in the third row of Figs 2–7. The continuous lines show the empirical limits that separate SF galaxies, AGN and HLR objects as defined by Riffel et al. (2013a) using the nuclear spectra of a large sample of galaxies. The HLR region corresponds to the highest values of [Fe II]1.2570 μm/Paβ and H$_2$ 2.1218 μm/Brγ line ratios, occupied by Transition Objects, LINERs and Supernovae Remnants. The H$_2$ flux maps show also emission from locations where no ionized gas emission is seen the H$_2$ emission is likely produced by shocks due to the interaction of a wide opening angle wind with the dense gas (e.g. Zakamska & Greene 2014; Riffel et al. 2020) or by X-rays from the central AGN escaping through the dusty torus. The former is in agreement with shock models used to describe the H$_2$ molecule formation from luminous galaxies (Guillard et al. 2009). For the latter one would expect the regions with H$_2$ emission and no ionized gas emission being located mainly perpendicular to the AGN ionization axis, which is not supported by the flux distributions in our sample. Similarly, there is [Fe II] emission in regions outside the AGN ionization cones, likely tracing the photodissociation regions at the cone edges.

Colina et al. (2015) presented a detailed analysis of the two-dimensional gas excitation in a sample of LIRGs and Seyfert nuclei using IFS spectroscopy and defined new areas in the near-IR
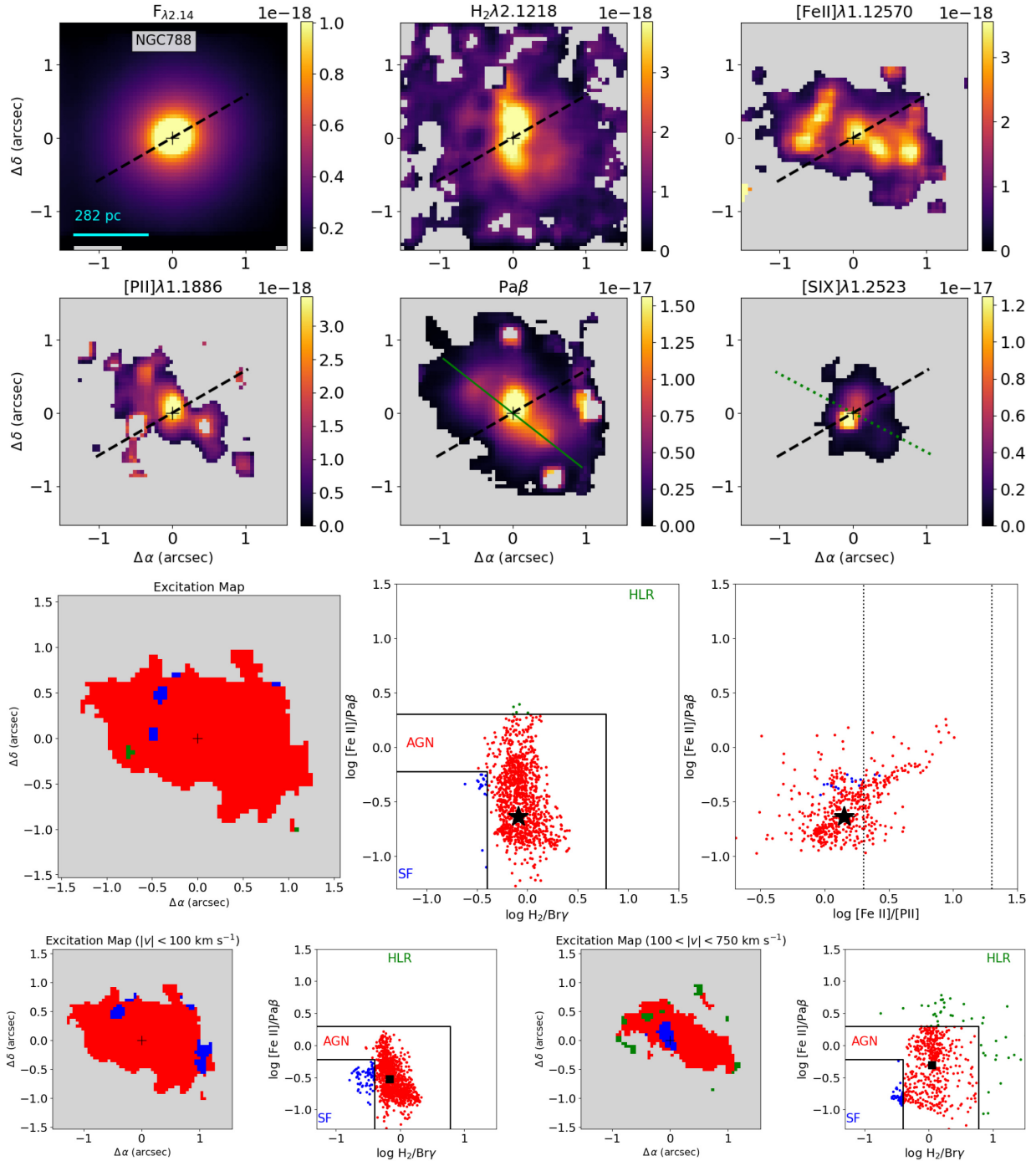
Figure 2. NGC 788 – first and second rows: Continuum emission measured from a *K*-band window and emission-line flux distributions for NGC 788. Grey regions correspond to locations where the emission lines are not detected at a 3σ continuum level, the crosses mark the location of the peak of the continuum emission and the dashed line corresponds to the orientation of the line of nodes derived by Riffel et al. (2017). The green continuous line shown in the Paβ map represents the orientation of the most collimated Paβ emission (which can be used as an indicator of the AGN ionization axis), computed using the CV2.MOMENTS python package. The green dotted line overplotted on the [S IX] image shows the orientation of radio emission from Nagar et al. (1999). The colour bars show the continuum in units of erg s^{-1} cm^{-2} Å^{-1} and the line fluxes in units of erg s^{-1} cm^{-2} of each spaxel. North is up and east is to the left. Third row: Emission-line ratio diagnostic diagrams for NGC 788. The left-hand panels show the excitation maps of the galaxy colour-coded according to the region in the [Fe II]1.2570 μm/Paβ versus H$_2$ 2.1218 μm/Brγ diagram, shown in the central panels. The lines delineating the SF, AGN, and high line ratio (HLR) regions are from Riffel et al. (2013a). The right panels show the [Fe II]1.2570 μm/Paβ versus [Fe II]1.2570 μm/[P II]1.1886 μm diagram using the same colour scheme from the excitation map. The central dotted vertical line corresponds to typical line ratios from photoionized ([Fe II]/[P II] = 2), while the right dotted vertical line corresponds to shock-dominated ([Fe II]/[P II] = 20) objects (Oliva et al. 2001; Storchi-Bergmann et al. 2009). The black stars show the line ratios within a circular aperture with radius of 0.5 arcsec. *Fourth row:* Excitation maps and [Fe II]1.2570 μm/Paβ versus H$_2$ 2.1218 μm/Brγ diagnostic diagrams for the low-velocity (|*v*| < 100 km s^{-1}: first and second panels) and high-velocity (100 km s^{-1} < |*v*| < 750 km s^{-1}: third and fourth panels) gas. The squares show the median line ratios.

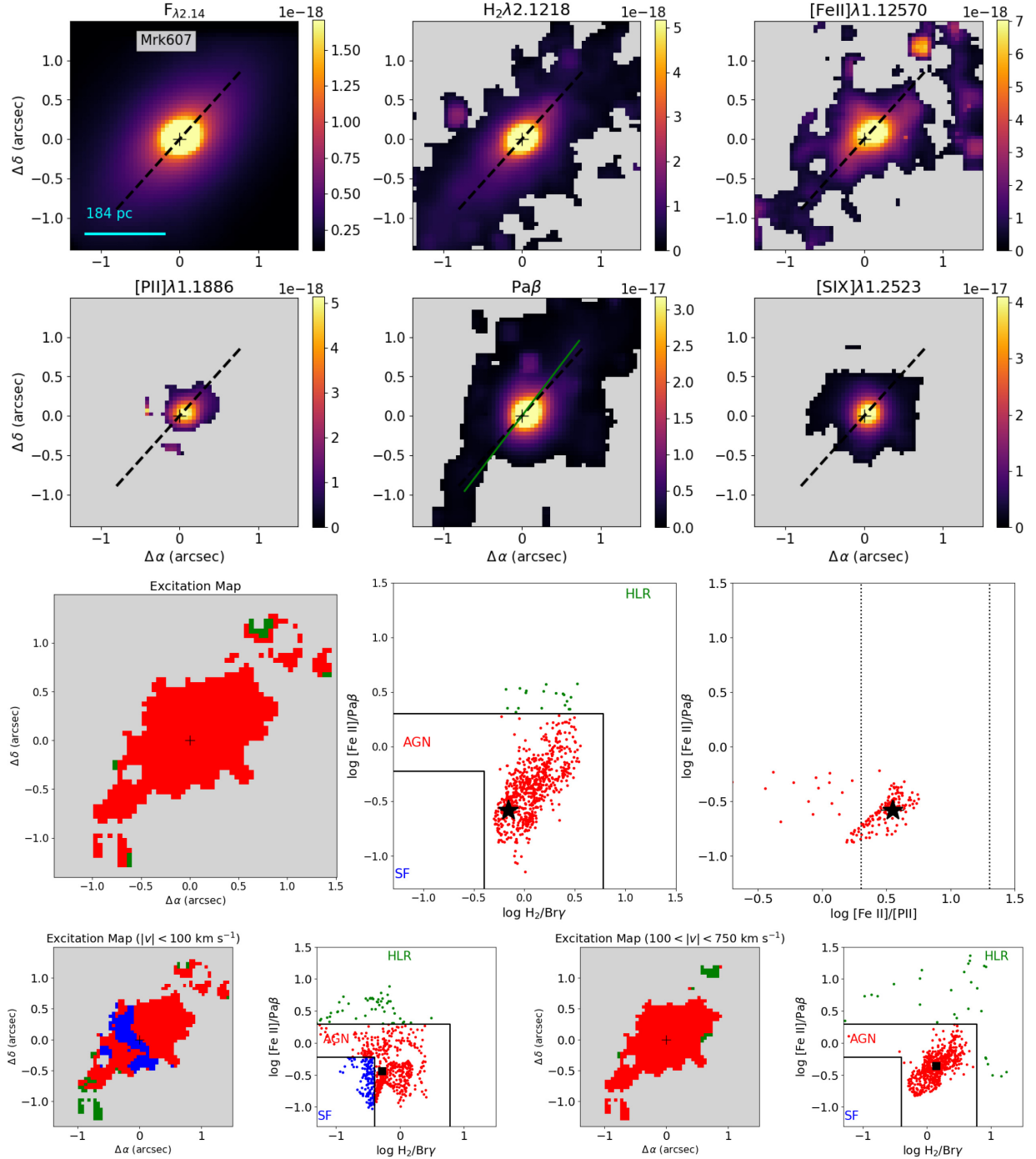**Figure 3.** Same as Fig. 2, but for **Mrk 607**.

diagnostic diagram for AGN, SF, and supernovae explosions. They used the [Fe II]1.6440 μm/Brγ and H$_2$ 2.1218 μm/Brγ line ratios, which can be converted to the ratios used in this work. Colina et al. (2015) used a similar range of values for the H$_2$ 2.1218 μm/Brγ to define the AGN region as that used in Riffel et al. (2013a), but their results indicate a larger upper limit of the [Fe II]1.2570 μm/Paβ (of ~7, obtained using the relation [Fe II]1.6440 μm/Brγ = 4.4974 × [Fe II]1.2570 μm/Paβ presented in their work). The sample of Seyfert galaxies used in Colina et al. (2015) is composed of only 5 objects and all of them present outflows that can produce shocks (Riffel et al. 2006a; Storchi-Bergmann et al. 2010; Riffel & Storchi-Bergmann

2011a,b; Riffel, Storchi-Bergmann & Winge 2013b; May et al. 2018, 2020), and thus, a contribution of shocks to the [Fe II] excitation cannot be ruled out. Thus, we used the separating lines from Riffel et al. (2013a), that even if they are based on single aperture spectra, these authors used a larger sample, composed of 67 galaxies.

The left panels in the third row of Figs 2–7 show the colour-coded excitation maps, where SF dominated spaxels are shown in blue, AGN dominated are in red and spaxels with line ratios in the HLR region are in green. All galaxies, but NGC 5506, show nuclear line ratios typical of AGN. NGC 788, Mrk 607 and NGC 3516 show line ratios in the AGN region of the diagnostic diagram in all locations,
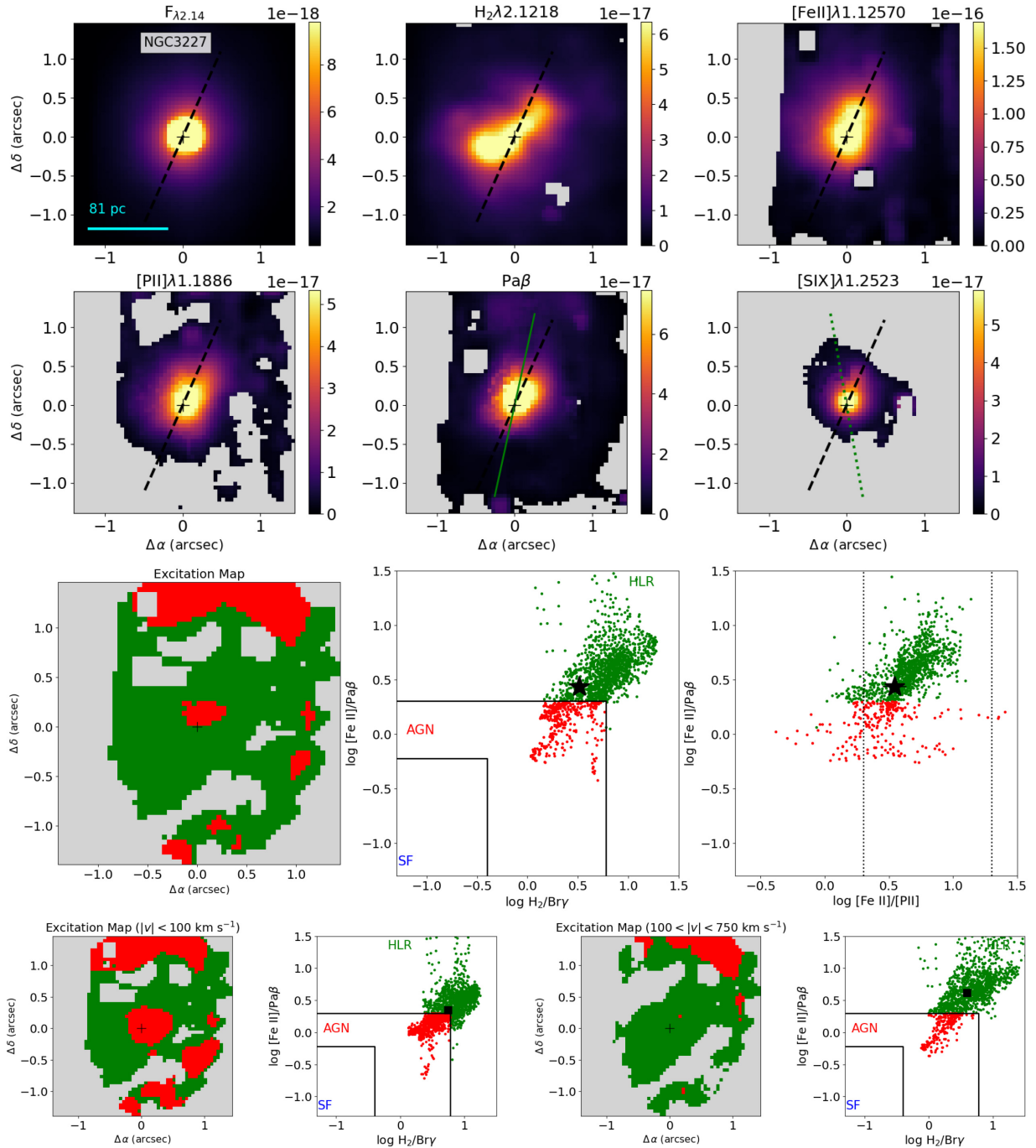
Figure 4. Same as Fig. 2, but for NGC 3227. The green dotted line overploted on the [S IX] image shows the orientation of radio emission from Mundell et al. (1995).

but the Brγ emission line is detected only at the centre in the latter. HLRs are seen in some locations for NGC 3227, NGC 5506 and NGC 5899. The only galaxy for which we found SF line ratios is NGC 5506, observed in the innermost region around the nucleus.

Another line ratio useful to investigate the role of shocks in the excitation of the [Fe II] is the [Fe II]1.2570 μm/[P II]1.1886 μm. This line ratio increases if shocks release the iron from dust grains reaching values of ∼20 in supernovae remnants, while values of ≲2 are seen in photoionized gas (Oliva et al. 2001; Storchi-Bergmann et al. 2009). Schönell et al. (2019) presented the [Fe II]/[P II] ratio maps for our

sample and here we present a plot of [Fe II]/Paβ versus [Fe II]/[P II] for the galaxy spaxels of our sample in the right-hand panels of the third row of Figs 2–7. The colour coding is the same as for the [Fe II]/Paβ versus H₂/Brγ diagram. The dotted vertical lines in these panels represent the limits of ratios in photoionized objects and in shock dominated objects – [Fe II]/[P II] = 2 and 20, respectively (Oliva et al. 2001; Storchi-Bergmann et al. 2009) – see also Riffel et al. (2019). All galaxies show ratios larger than 2, with the highest values corresponding to the HLR regions in the excitation maps shown in the bottom left-hand panels of Figs 2–7.
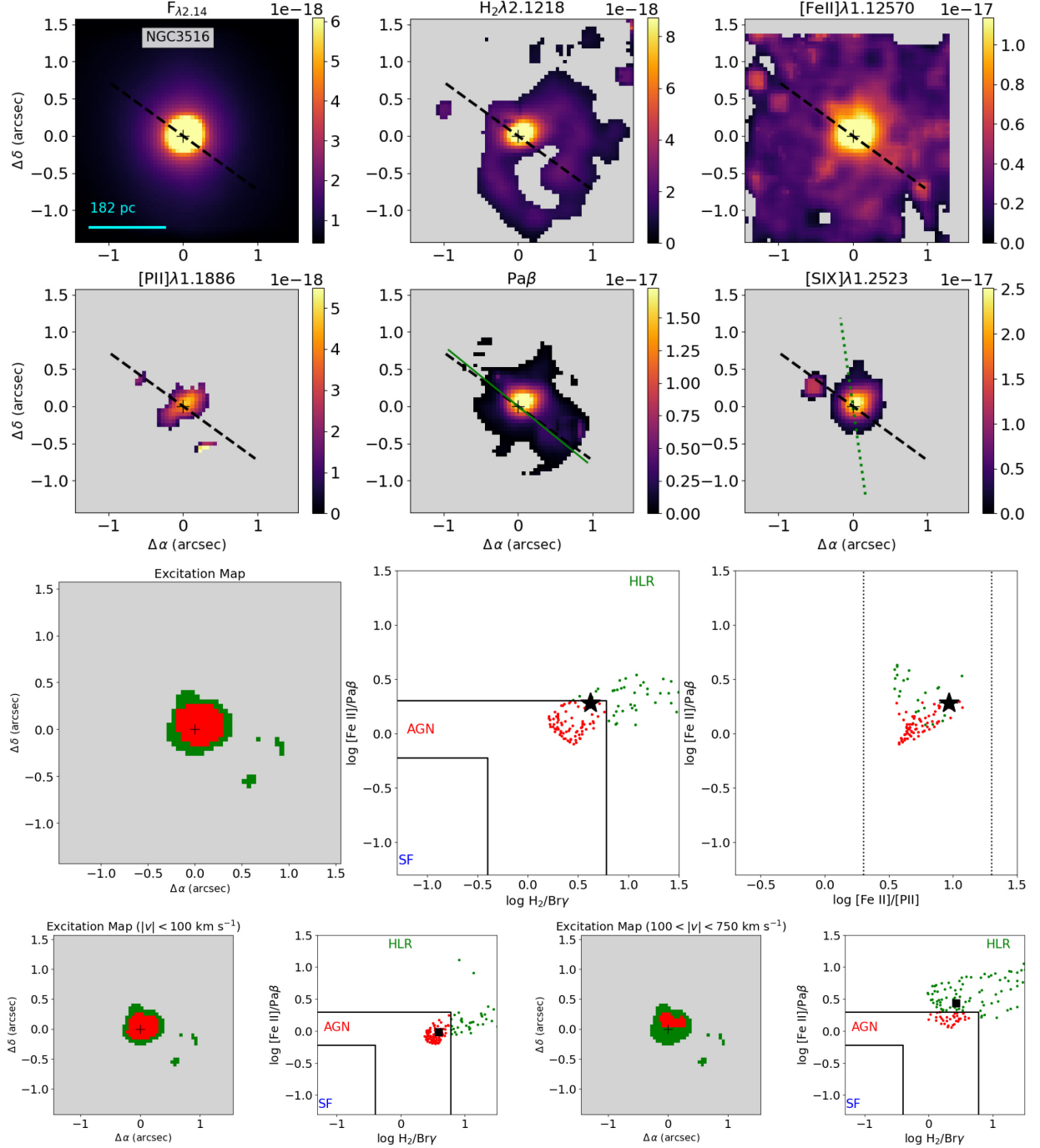
Figure 5. Same as Fig. 2, but for NGC 3516. The green dotted line overploted on the [S IX] image shows the orientation of radio emission from Nagar et al. (1999).

Table 1 presents the emission-line ratios, measured within two distinct apertures: (i) within the 100 pc radius and (ii) within 0.5 arcsec radius. The first aperture allows the comparison of the line ratios observed in distinct galaxies at the same physical scale, while the latter is useful to investigate the nuclear line emission.

The bottom row of Figs 2–7 show the excitation maps and diagnostic diagrams for each galaxy, constructed using the line fluxes integrated within two velocity ranges: (i) the low-velocity range $|v| < 100\,\mathrm{km\,s^{-1}}$ and (ii) the high-velocity range $100\,\mathrm{km\,s^{-1}} <$

$|v| < 750\,\mathrm{km\,s^{-1}}$. The velocity range in each spaxel is measured relative to the velocity of the peak of the corresponding line profile. The high-velocity range is more sensitive to shock excitation, as observed in optical emission lines (e.g. Ho et al. 2014; D'Agostino et al. 2019b; Riffel et al. 2021). We exclude from these diagrams spaxels where the emission lines are not detected at a 3σ continuum level.

The H$_2$ 2-1 S(1)2.2477 µm/1-0 S(1)2.1218 µm versus 1-0 S(2)2.0338 µm/1-0 S(0)2.2235 µm diagram is useful to investigate the origin of the H$_2$ emission. The spectral range for Mrk 607 and
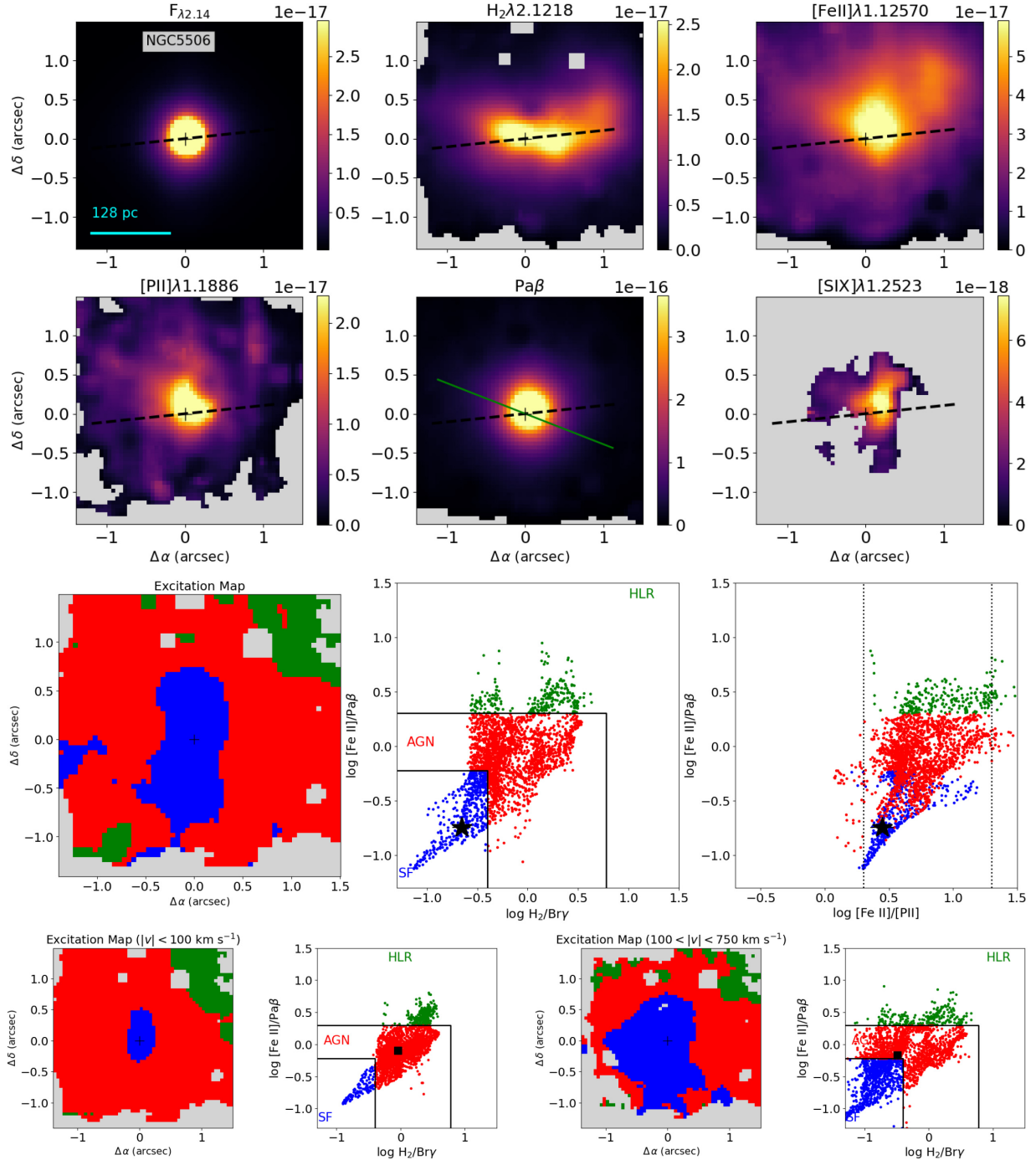
Figure 6. Same as Fig. 2, but for NGC 5506.

NGC 5899 does not include the H_2 2.0338 µm emission line and these lines are not detected in our data of NGC 3516. Thus, we construct the H_2 diagnostic diagrams only for NGC 788, NGC 3227 and NGC 5506 and present them in Fig. 8. The colours of the points are defined as in Figs 2–7 and we show also in the figure the predictions of distinct models. Most points in the diagrams for the three galaxies are away from the region predicted by the non-thermal UV excitation models of Black & van Dishoeck (1987) (identified by the orange polygon), indicating that the H_2 emission originates in thermal processes.

3.3 Molecular hydrogen temperatures

Fig. 9 presents the vibrational ($T_{\rm vib}$) and rotational ($T_{\rm rot}$) temperature distributions of the H_2 gas. These temperatures are obtained using the fluxes of the H_2 lines according to

$$T_{\rm vib} \cong \frac{5600}{\ln\left(1.355\frac{F_{H_2 2.1218\mu m}}{F_{H_2 2.2477\mu m}}\right)}. \tag{1}$$

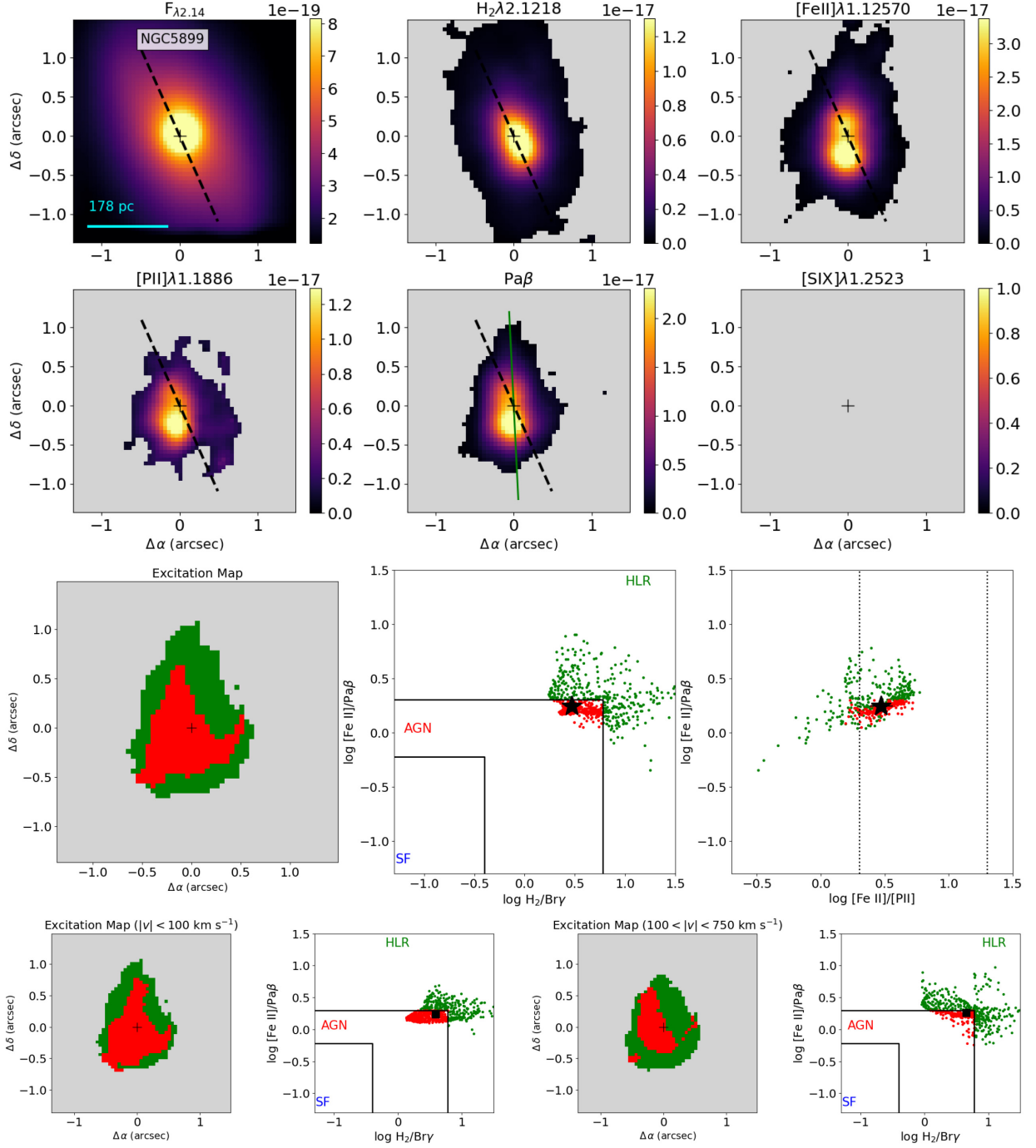**Figure 7.** Same as Fig. 2, but for NGC 5899.

Table 1. [Fe II]1.2570 µm/Paβ, [Fe II]1.2570 µm/[P II]1.1886 µm, [S IX]1.2523 µm/Paβ and H₂ 2.1218 µm/Brγ emission-line ratios computed within circular apertures of 100 pc and 0.5 arcsec radii.

| Galaxy	Aperture of 100 pc radius				Aperture of 0.5 arcsec radius			
	[Fe II]/Paβ	[Fe II]/[P II]	[S IX]/Paβ	H₂/Brγ	[Fe II]/Paβ	[Fe II]/[P II]	[S IX]/Paβ	H₂/Brγ
NGC 788	0.18 ± 0.05	1.15 ± 0.55	0.39 ± 0.16	0.71 ± 0.25	0.23 ± 0.03	1.41 ± 0.33	0.32 ± 0.07	0.81 ± 0.14
Mrk607	0.26 ± 0.03	2.98 ± 0.57	0.75 ± 0.13	0.70 ± 0.11	0.26 ± 0.03	3.53 ± 0.82	0.76 ± 0.17	0.69 ± 0.13
NGC 3227	3.44 ± 0.05	5.12 ± 0.15	0.66 ± 0.11	5.12 ± 0.27	2.71 ± 0.35	3.5 ± 0.82	0.42 ± 0.09	1.44 ± 0.25
NGC 3516	1.70 ± 0.24	8.50 ± 1.98	1.23 ± 0.25	4.40 ± 0.64	1.9 ± 0.24	9.28 ± 1.79	1.26 ± 0.22	4.19 ± 0.73
NGC 5506	0.25 ± 0.05	3.46 ± 0.32	0.011 ± 0.002	0.28 ± 0.05	0.18 ± 0.02	2.81 ± 0.66	0.011 ± 0.004	0.22 ± 0.05
NGC 5899	1.72 ± 0.18	3.07 ± 0.59	0.001 ± 0.001	3.03 ± 0.25	1.75 ± 0.23	2.97 ± 0.69	0.001 ± 0.001	2.94 ± 0.51
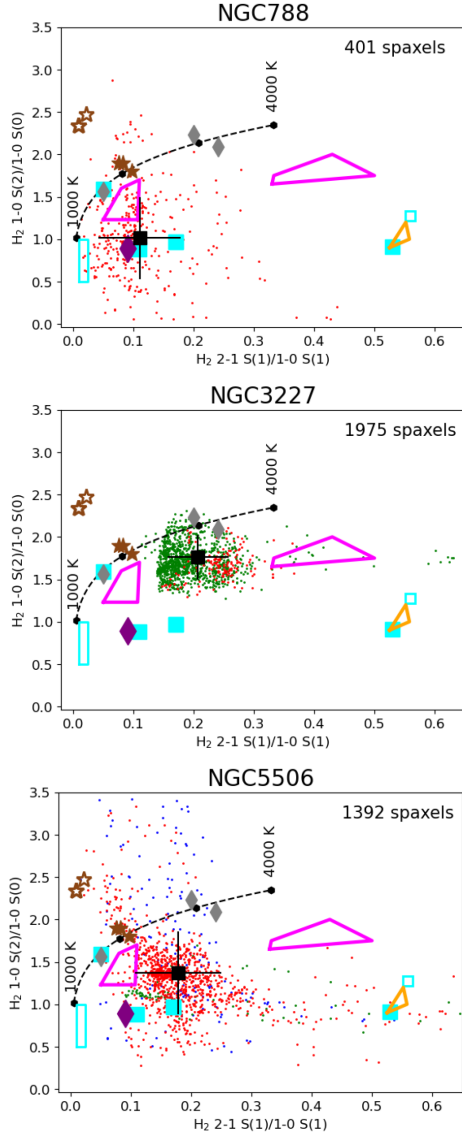
Figure 8. H$_2$ 2–1 S(1)2.2477 µm/1–0 S(1)2.1218 µm versus 1–0 S(2)2.0338 µm/1–0 S(0)2.2235 µm diagnostic diagram for NGC 788, NGC 3227 and NGC 5506. The colours of the points represent the different regions identified in the diagnostic diagrams of Figs 2, 4 and 6. The black dashed curve corresponds to the ratios for an isothermal and uniform density gas distribution for temperatures ranging from 1000 to 4000 K, rom left- to right-hand side. The open cyan rectangle shows the regions predicted from the thermal UV excitation models of Sternberg & Dalgarno (1989) for gas densities (n_t) between 10^5 and 10^6 cm^{-3} and UV scaling factors relative to the local interstellar radiation field χ from 10^2 to 10^4, as computed by Mouri (1994). The open cyan square is from Sternberg & Dalgarno (1989) for $n_t = 10^3$ cm^{-3} and $\chi = 10^2$ and the filled cyan squares are the UV thermal models from Davies et al. (2003) with $10^3 < n_t < 10^6$ cm^{-3} and $10^2 < \chi < 10^5$. The brown open and filled stars are from the thermal X-ray models of Lepp & McCray (1983) and Draine & Woods (1990), respectively. The purple diamond is from the shocks model of Kwan et al. (1977) and the grey diamonds represent the shock models from Smith (1995). The orange polygon represents the region occupied by the non-thermal UV excitation models of Black & van Dishoeck (1987) and the open magenta polygons cover the region of the photoionization models of Dors et al. (2012). We do not overlay the predictions of the photoionization from Riffel et al. (2013a), as they span a wide range in both axes ($0 \lesssim 2$–1 S(1)/1–0 S(1) $\lesssim 0.6$ and $0.5 \lesssim 1$–0 S(2)/1–0 S(0) $\lesssim 2.5$). The black squares with error bars show the median line ratios and standard deviations for each galaxy.

and

$$T_{\rm rot} \cong -\frac{1113}{\ln\left(0.323 \frac{F_{H_2 2.0338 \mu m}}{F_{H_2 2.2235 \mu m}}\right)}, \qquad (2)$$

respectively (Reunanen et al. 2002) and the Einstein coefficients are taken from Turner, Kirby-Docken & Dalgarno (1977). As mentioned above, for Mrk 607 and NGC 5899 the spectral range does not include the H$_2$ 2.0338 µm emission line and thus we do not estimate the H$_2$ rotational temperatures for these galaxies. Although the spectral region of the NGC 3516 data includes the H$_2$ 2.0338 µm emission line, the signal-to-noise ratios in both lines used to derive the rotational temperature are not high enough to obtain $T_{\rm rot}$, so we also present only the vibrational temperature map for this galaxy. The grey regions in the maps of Fig. 9 correspond to locations where one or both emission lines used to calculate the corresponding temperature are not detected with, at least, 2σ above the noise level with respect to the adjacent continuum.

The vibrational temperatures range from ∼1000 to ∼5000 K, while the rotational temperatures range from a few hundred to ∼4000 K. Overall, NGC 788 shows much smaller values of $T_{\rm rot}$ than those of $T_{\rm vib}$, while for NGC 3227 both temperature ranges are similar and for NGC 5506 $T_{\rm rot}$ is slightly smaller than $T_{\rm vib}$. Table 2 presents temperature values estimated within circular apertures of 100 pc and 0.5 arcsec radii, centred at the nuclei of the galaxies.

4 DISCUSSION

4.1 Notes on individual objects

4.1.1 NGC 788

NGC 788 is a spiral galaxy (SA0/a?(s)) located at 56 Mpc and hosts a Sy 2 nucleus. The stellar velocity field is described by a rotation pattern, with the orientation of the line of the nodes $\Psi_0 \sim 120°$ and smaller (∼50 − 80 km s^{-1}) stellar velocity dispersion patches are observed at 250 pc, probably due to intermediate age stellar populations (Riffel et al. 2017). The radial profile for the ionized gas mass is more concentrated in the centre (∼100 pc) and has a steeper distribution than that of the hot molecular gas (Riffel et al. 2018). By mapping the gas distribution, Schönell et al. (2019) show that Paβ and [Fe II] 1.2570 µm emission are extended along the northeast–southwest direction and present higher (∼150 km s^{-1}) velocity amplitudes and regions of $\sigma \sim 150$ km s^{-1} in the same direction, interpreted as a bipolar outflow. On the other hand, the H$_2$ 2.1218 µm presents emission in the whole NIFS FoV and low-velocity dispersion ($\sigma \sim 50$ km s^{-1}). NGC 788 presents a compact radio emission at 3.6 cm and slightly resolved extended radio emission along the position angle PA = 62° at 20 cm (Nagar et al. 1999).

Our results are shown in Fig. 2. The [Fe II]1.2570 µm flux distribution is more extended along the NE-SW direction and presents several knots of enhanced emission. Similar orientations and knots of emission are also observed in Paβ and [P II]. The ionized gas emission is likely tracing the AGN ionization structure. We find that the Paβ emission is extended mostly along PA = 52° ± 4°, which is displaced from stellar kinematic PA (120° ± 3°; Riffel et al. 2017) by ∼68°. The highest intensity levels in the H$_2$ flux map are more extended along the N–S direction, while at lower flux levels, the H$_2$ emission spreads over the whole NIFS FoV. The [S IX]1.2523 µm is compact and slightly elongated along the AGN ionization axis, as traced by the orientation of the Paβ emission. The H$_2$ 2.1218 µm/Brγ versus [Fe II]1.2570 µm/Paβ diagnostic diagram of NGC 788 shows all values in the AGN region, but the [Fe II]/Paβ
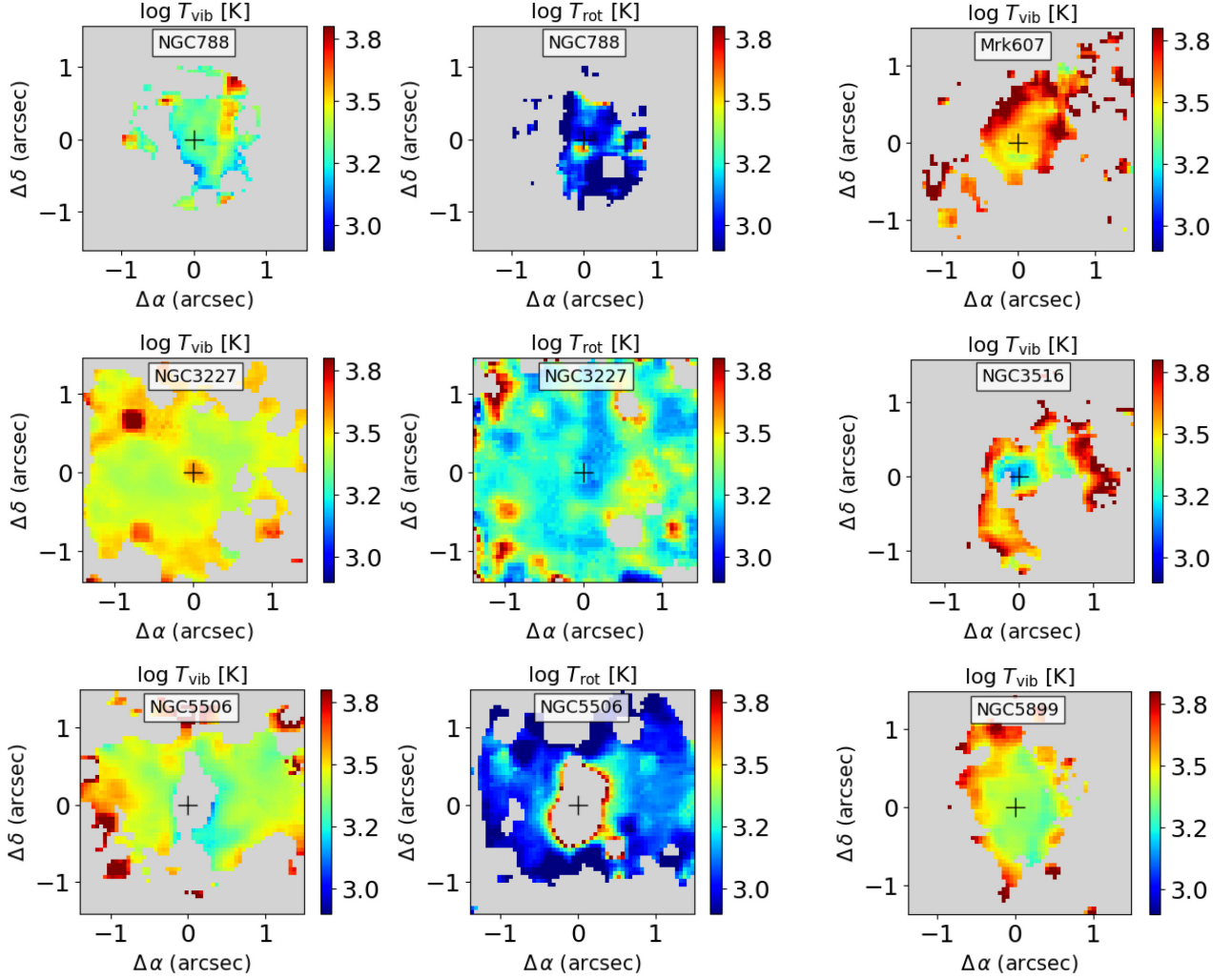
Figure 9. H_2 vibrational and rotational temperatures of NGC 788, NGC 3227, and NGC 5506 calculated according to equations (1) and (2). For Mrk 607, NGC 3516, and NGC 5899 only the vibrational temperature is presented because the H_2 2.0338 μm line is not detected in these galaxies. The grey regions indicate the spaxels where at least one of the H_2 emission lines is not detected within 2σ above the continuum noise.

Table 2. H_2 vibrational and rotational temperatures computed within circular apertures of 100 pc (columns 2 and 3) and 0.5 arcsec (columns 4 and 5) radius.

Galaxy	$T_{vib:r\leq100\,pc}$ (K)	$T_{rot:r\leq100\,pc}$ (K)	$T_{vib:r\leq0.5\,arcsec}$ (K)	$T_{rot:r\leq0.5\,arcsec}$ (K)
NGC 788	2145 ± 308	1126 ± 963	2276 ± 201	1073 ± 339
Mrk 607	3634 ± 419	–	3370 ± 422	–
NGC 3227	3069 ± 69	1745 ± 130	2864 ± 313	1723 ± 820
NGC 3516	2546 ± 213	–	2431 ± 228	–
NGC 5506	2055 ± 72	1485 ± 242	1602 ± 102	1528 ± 860
NGC 5899	2438 ± 196	–	2525 ± 245	–

ratio is smaller than 2.0 at most locations. The [Fe II]/[P II] ratio is also smaller than 2.0 at most locations. The Spearman test reveals that there is no correlation between H_2/Brγ and [Fe II]/Paβ. The median value of the [Fe II]/Paβ for the high-velocity range is larger than that of the low-velocity range.

4.1.2 Mrk 607

Mrk 607 is an edge-on spiral galaxy ($i = 70°$) classified as Sa?, hosts a Seyfert 2 nucleus and is located at ≈37 Mpc (Véron-Cetty &

Véron 2006). *Hubble Space Telescope* (*HST*) observations show that the [O III] emission is well aligned to the galaxy's major axis (PA ≈ −43°), being more extended along the north-east side (Ferruit, Wilson & Mulchaey 2000; Schmitt et al. 2003). Patches of low stellar velocity dispersion produced by young to intermediate age stellar populations are observed at distances of 200 pc from the centre (Riffel et al. 2017). Optical and near-IR IFS observations show that the stellar kinematics in the inner kpc of Mrk 607 is dominated by rotation in the plane of the disc. The gas also presents a clear rotation pattern, but in the opposite direction of the stars (Riffel et al. 2017;

Freitas et al. 2018; Schönell et al. 2019). In addition, equatorial ionized outflows (perpendicular to the ionization cone) are observed in the optical emission lines (Freitas et al. 2018). Radio emission is seen only from a nuclear compact source, with no evidence of a radio jet at kpc scales (Colbert et al. 1996; Nagar et al. 1999).

For Mrk 607 (Fig. 3), we find that the molecular and ionized gas emission is more extended along the orientation of line of nodes derived from the stellar velocity line of nodes (138° ± 3°; Riffel et al. 2017). The ionized gas is more extended to the north-west side of the nucleus and we derive an orientation for the Paβ emission of 143° ± 4°, consistent with the stellar kinematic PA and with the orientation of optical emission (Ferruit et al. 2000; Schmitt et al. 2003; Freitas et al. 2018). The [P II]1.1886 μm and [S IX]1.2523 μm show emission only at distances smaller than 0.8 arcsec from the nucleus. As for NGC 788, the H_2/Brγ versus [Fe II]/Paβ diagnostic diagram shows all values in the AGN region, but a good correlation is found between both ratios. The [Fe II]/[P II] ratio is larger than 2.0 at most locations, reaching values of up to ∼7. Both the H_2/Brγ and [Fe II]/Paβ ratios median values are larger for the high-velocity range, compared to the low-velocity gas. Values typical of SF galaxies are seen for the low-velocity range in a narrow stripe perpendicular to the galaxy's major axis, co-spatial with the equatorial outflows observed in ionized gas (Freitas et al. 2018).

4.1.3 NGC 3227

NGC 3227 is a spiral galaxy (SAB(s)a), located at a distance of 22 Mpc and with a Sy 1.5 nucleus (Ho, Filippenko & Sargent 1997). A full description of its NIR emission line spectrum is made in Riffel et al. (2006b). Radio continuum observations at 18 cm show two main components separated by 0.4 arcsec, offset from the optical peak and located at PA ≈ −10°. An outflow is observed in the [O III]5007 Å, but it is not aligned with the radio emission (Mundell et al. 1995). Signatures of outflows are also observed in Hα (Arribas & Mediavilla 1994) and in H_2 1-0S(1) in the central 1−2 arcsec (Davies et al. 2014). Schinnerer, Eckart & Tacconi (2000) detected an asymmetric nuclear ring of cold molecular gas with 3 arcsec diameter, which is co-spatial with regions of high [Fe II]/Paβ (of up to 4) and H_2/Brγ (up to 10) values (Schönell et al. 2019). The velocity fields of the hot molecular and ionized gas show a rotation pattern, but it is distorted indicating the presence of additional kinematic components (Schönell et al. 2019).

The flux maps for NGC 3227 (Fig. 4), show extended emission over most of the FoV, except for the [S IX]1.2523 μm, whose emission is restricted to the inner ∼1 arcsec radius. The flux distributions are more elongated along the galaxy's major axis (156° ± 3°; Riffel et al. 2017) and we derive an orientation of 168° ± 6° for the Paβ emission, which close to the orientation of the radio jet (Mundell et al. 1995), and thus it is likely tracing the AGN ionization axis. The H_2/Brγ versus [Fe II]/Paβ diagram shows values in the AGN and HLR regions, with the AGN ratios seen mainly at the centre and close to the borders of the FoV, along the AGN ionization axis. The [P II]/Paβ line ratio presents values between 2 and 15 in most locations and it correlates with the [Fe II]/Paβ. The excitation map for the low-velocity range highlights the structure seen in the excitation map using the total fluxes, with values typical of AGN at the nucleus and along the AGN ionization axis, and HLRs in between. On the other hand, for the high-velocity range, most of the ratios fall in the HLR region, except for a region northern of the nucleus, close to the border of the NIFS FoV. As for the previous galaxies, the median line ratios for the high-velocity range are larger than those for the low-velocity gas.

4.1.4 NGC 3516

This is a lenticular galaxy, classified as (R)SB0⁰?(s), with a Sy 1.2 nucleus. Recently a detection of a UV flare placed this galaxy as a changing-look AGN (Ilić et al. 2020). The gas velocity fields deviate from a well-behaved rotation pattern, as observed for the near-IR emission lines (Schönell et al. 2019) and Hα (Veilleux, Tully & Bland-Hawthorn 1993). This feature is likely due to a bipolar outflow (Goad & Gallagher 1987) and explained by a precessing twin jet model (Veilleut et al. 1993). Schönell et al. (2019) reported [Fe II]1.257 μm/Paβ > 2 in regions with enhanced $\sigma_{[Fe II]}$ values (∼150 km s⁻¹), indicating shocks. As is the case of Mrk 607, NGC 3516 presents patches of smaller stellar velocity dispersion values (∼50−80 km s⁻¹) due to the presence of young to intermediate stellar populations. An extended radio emission along PA ≈ 8° is detected at 20 cm, while at 3.6 cm only unresolved nuclear emission is detected (Nagar et al. 1999). The [O III] emission observed by *HST* shows an S-shaped morphology, extended by 13.6 arcsec along PA ≈ 20° (Schmitt et al. 2003).

The emission-line flux distributions for NGC 3516 (Fig. 5) are the most compact among all galaxies in our sample. Only the [Fe II] presents emission over the whole FoV. The extended emission is seen mainly along the major axis of the galaxy (54° ± 3°; Riffel et al. 2017). We derive an orientation of 51° ± 7° for the Paβ emission, which may be tracing emission from the galaxy's disc rather than the AGN ionization structure, as at larger scales, this galaxy presents a clear extended NLR along PA ≈ 20° (Schmitt et al. 2003). Not much can be said about the ionization structure of this galaxy, as we were able to measure all emission lines only at the centre. The observed line ratios fall in the AGN and HLR regions of the diagnostic diagram, and higher median values are found for the line ratios using the high-velocity range, as compared to those of the low-velocity range.

4.1.5 NGC 5506

NGC 5506 is a spiral galaxy classified as Sa pec edge-on, located at a distance of 31 Mpc and hosting a Sy 1.9 nucleus (Blanco, Ward & Wright 1990; Kewley et al. 2001). NIFS observations of NGC 5506 show that [Fe II]1.257 μm flux distribution is more extended perpendicularly to the galaxy's major axis ($\Psi_0 = 90°$) (Riffel et al. 2017; Schönell et al. 2019). This feature, combined with structures in the same spatial location with high-velocity dispersion (∼300 km s⁻¹) and the distorted velocity fields, supports the presence of an ionized gas outflow, previously observed using optical long-slit spectra (Maiolino et al. 1994). The H_2 2.1218 μm is distributed along the major axis and its emission is not as prominent as for the ionized gas, this is probably because the H_2 molecule is dissociated by AGN radiation (Schönell et al. 2019). VLA observations of NGC 5506 at 3.6 cm reveal a linear structure along the east-west direction, surrounded by diffuse emission, with a total extension of 300 pc (Schmitt et al. 2001).

The [Fe II] flux distribution of NGC 5506 (Fig. 6) shows a well-defined one-sided cone to the north of the nucleus, which is also seen in the [P II] flux map. The H_2 flux distribution is more elongated along the galaxy's major axis (96° ± 3°; Riffel et al. 2017), presenting a structure that seems to be tracing the outer walls of the cone seen in [Fe II]. The Paβ shows a round flux distribution and we derive an orientation of 67° ± 4°, which seems to trace the east wall of the cone seen in [Fe II]. The [S IX] line emission is slightly more extended to the north of the nucleus. The H_2/Brγ versus [Fe II]/Paβ shows values in all regions, with values typical of SF at the nucleus and along the north–south direction, surrounded by the values typical

of AGN and HLRs are seen close to the borders of the NIFS FoV. A good correlation is found between H₂/Brγ and [Fe II]/Paβ, and between [Fe II]/Paβ and [Fe II]/[P II], with the latter ratio presenting values of up to 20. Unlike previous objects, this galaxy presents smaller line ratios for the high-velocity gas than for the low-velocity range. This behaviour will be further discussed in next section.

4.1.6 NGC 5899

NGC 5899 is located at 39 Mpc, classified as SAB(rs)c (Ann, Seo & Ha 2015) and hosts a Sy 2 nucleus (de Vaucouleurs et al. 1991). This galaxy presents a partial ring of low stellar velocity dispersion (50−80 km s⁻¹) with radius of 200 pc centred at the galaxy nucleus likely produced by young/intermediate age stellar populations (Riffel et al. 2017). Schönell et al. (2019) found that the H₂ 2.1218 μm emission is extended along the galaxy major axis (PA = 25°) and shows a rotation pattern with small velocity dispersion values over the whole field of view. On the other hand, the strongest [Fe II] 1.2570 μm and Paβ emissions are seen along the north–south direction, as well as the highest gradient in the velocity fields. The velocity dispersion of the [Fe II] reaches values of ∼300 km s⁻¹ reinforcing the hypothesis that the ionized gas traces an outflow, while the molecular gas follows the rotation of the stars (Schönell et al. 2019). To the best of our knowledge, no extended radio emission is detected in NGC 5899.

The H₂ emission in NGC 5899 (Fig. 7) is more extended along the orientation of the galaxy's disc (24° ± 3°; Riffel et al. 2017), while the ionized gas is displaced by 23° from it, and the emission peak of the ionized gas emission is observed at 0.3 arcsec south of the nucleus. No [S IX]1.2523 μm emission is detected spaxel-by-spaxel, but we were able to measure its flux using integrated spectra, as shown in Table 1. The excitation map shows values in the AGN region, close to the nucleus, surrounded by HLR regions. There is no correlation between H₂/Brγ and [Fe II]/Paβ, but the range of values observed in both line ratios is small. At most locations, the [Fe II]/[P II] is slightly larger than 2. The median H₂/Brγ and [Fe II]/Paβ ratios for the low and high-velocity ranges are similar, but the fraction of spaxels in the HLR is larger for the latter.

4.2 Gas excitation

The most comprehensive study of the two-dimensional ionization structure in nearby galaxies using near-IR IFS was performed by Colina et al. (2015). The authors used the H₂ 2.1218 μm/Brγ and [Fe II] 1.6440 μm/Brγ diagnostic diagram, as their VLT SINFONI data covers the *H* and *K* bands. The diagnostic diagrams are presented for 10 LIRGs and are compared with results from previously published data of SF and Seyfert galaxies. The results in Colina et al. (2015) indicates that H₂ 2.1218 μm/Brγ and [Fe II] 1.6440 μm/Brγ are correlated in most objects (e.g. IC 4687), while no correlations are observed in few objects (e.g. NGC 3256). As the SINFONI covers a larger FoV than NIFS and the ionization structure in LIRGS is more complex, most of objects in the sample of Colina et al. (2015) show line ratios spanning a wide range of values. Some of the Seyfert galaxies in their work clearly show no correlation between the line ratios involved in the diagnostic diagram (e.g. Mrk 1157; Riffel & Storchi-Bergmann 2011b). We find strong correlations between H₂ 2.1218 μm/Brγ and [Fe II]1.2570 μm/Paβ for Mrk 607, NGC 3227 and NGC 5506, while no correlations are found for the other galaxies, although a trend of increasing H₂/Brγ with the increasing of [Fe II]/Paβ is observed for NGC 3516 (but the number of points is small) and for the high-velocity range of NGC 788.
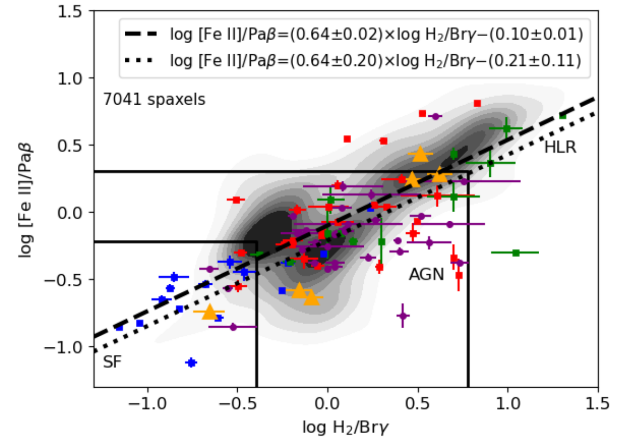

Figure 10. Density plot for the [Fe II]1.2570 μm/Paβ versus H₂ 2.1218 μm/Brγ diagram for our sample. The lines delineating the SF, AGN and HLR regions are from Riffel et al. (2013a) and the dashed line shows the best linear fit of the data. The SF, AGN, and HLR regions contain 7, 64, and 29 per cent of the points, respectively. The contour levels are equally separated in steps of 10 per cent of the total number of spaxels. The colour points represent line ratios from single aperture spectra compiled from the literature. The squares are from measurements by Larkin et al. (1998), Knop et al. (2001), Reunanen et al. (2002), Dale et al. (2004), Rodríguez-Ardila et al. (2004, 2005), Riffel et al. (2006b, 2013a), Izotov & Thuan (2011) – blue squares represent SF and blue compact dwarf galaxies, red squares are Seyfert nuclei and green squares represent LINERs. BAT AGN from Lamperti et al. (2017) are shown as purple circles. Measurements for our sample within 0.5 arcsec radius are shown as orange triangles. The dotted line represents the best linear fit using the integrated line ratios.

However, considering that the SINFONI data used in Colina et al. (2015) covers a larger FoV, their observations are seeing limited and their sample has an average redshift larger than ours, a comparison between individual correlations is not straightforward.

We use the emission-line ratios of all galaxies of our sample to construct the [Fe II]1.2570 μm/Paβ versus H₂ 2.1218 μm/Brγ diagnostic diagram (shown in Fig. 10), which is useful to investigate the origin of the near-IR emission lines. We find a strong correlation between [Fe II]/Paβ and H₂/Brγ in good agreement with previous results using single aperture (e.g. Rodríguez-Ardila et al. 2005; Riffel et al. 2013a) and integral field (e.g. Colina et al. 2015) spectra of nearby active galaxies. As the Paβ and Brγ emission lines are originated from the same process (i.e. photoionization by the AGN or young-massive stars), a possible interpretation of this correlation is that the H₂ and [Fe II] emissions originate from the same excitation mechanism.

We use a Spearman correlation test and find a correlation coefficient between [Fe II]/Paβ and H₂/Brγ of $R_p = 0.68$ and a correlation confidence level larger than 99.9 per cent. This suggests that the [Fe II] and H₂ emissions in our sample are dominated by thermal processes. We fit the data by a linear equation resulting in

$$\log\left(\frac{[\text{Fe II}]}{\text{Pa}\beta}\right) = (0.65 \pm 0.026)$$
$$\times \log\left(\frac{\text{H}_2}{\text{Br}\gamma}\right) - (0.12 \pm 0.013). \quad (3)$$

The best-fitting equation to our data is shown as a dashed line in Fig. 10, which is consistent with the one obtained by Riffel et al. (2013a) using single aperture spectra of 67 nearby galaxies [$\log\frac{[\text{Fe II}]}{\text{Pa}\beta} = (0.749 \pm 0.072) \times \log\frac{\text{H}_2}{\text{Br}\gamma} - (0.207 \pm 0.046)$].
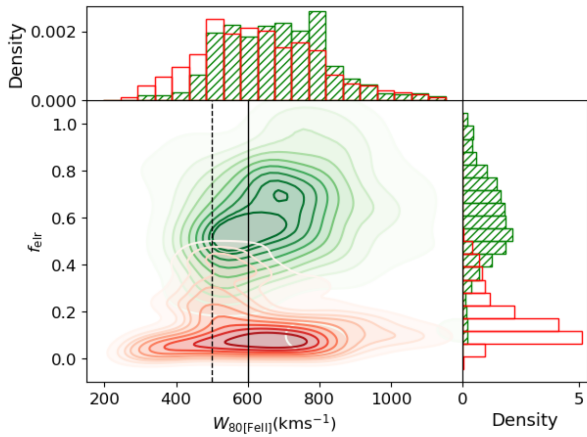
Figure 11. Emission-line ratio function versus $W_{80[FeII]}$ as defined by the equation (4). Red and green contours are from AGN and HLR regions identified in Figs 2–7. The contours are separated in steps of 10 per cent of the total number of spaxels. The vertical lines identify the lower limits of W_{80} (500 and 600 km s^{-1}) in ionized outflows.

We have also compiled the [Fe II]/Paβ and H$_2$/Brγ ratios measured by integrated spectra for a sample of 93 objects composed of SF Galaxies (Larkin et al. 1998; Dale et al. 2004; Rodríguez-Ardila et al. 2005; Riffel et al. 2013a), Blue Compact Dwarf Galaxies (Izotov & Thuan 2011), Seyfert galaxies (Knop et al. 2001; Reunanen et al. 2002; Rodríguez-Ardila et al. 2004, 2005; Riffel et al. 2006b), LINERs (Larkin et al. 1998; Riffel et al. 2013a) and BAT AGN (Lamperti et al. 2017). We show these measurements as colour points in Fig. 10 and include the nuclear ratios observed in our sample, within 0.5 arcsec radius, represented by the orange triangles. As already noticed in Riffel et al. (2013a), there is a strong correlation between the nuclear [Fe II]/Paβ and H$_2$/Brγ ratios. The Spearman test results in $R_p = 0.66$ and p-value $= 9.6 \times 10^{-14}$. It is worth mentioning that the correlation coefficients for the integrated and spatially resolved line ratios are very similar, meaning that the [Fe II]/Paβ and H$_2$/Brγ diagnostic diagram, originally designed for single aperture measurements, can be used to obtain information on the excitation of the spatially resolved emitting gas. The best linear fit of the single aperture data, shown as a dotted line Fig. 10, is well consistent with the resulting fit of the spatially resolved data (dashed line).

Except for NGC 5506, all galaxies show higher line ratios in the high-velocity range (100 km s^{-1} < |v| < 750 km s^{-1}) than in the low-velocity range |v| < 100 km s^{-1}). This indicates that shocks contribute to the [Fe II] and H$_2$ emission, even in galaxies with most of the spaxels in the AGN region of the diagnostic diagrams (e.g. NGC 788 and Mrk 607).

In order to further investigate the origin of the line emission, we use two quantities that can be obtained from our data: W_{80} and f_{elr}. W_{80} is the width of an emission-line above which 80 per cent of the flux is emitted, and is frequently used to identify ionized outflows (Zakamska & Greene 2014; Wylezalek et al. 2017, 2020; Kakkad et al. 2020; Riffel et al. 2020). The W_{80} parameter is more sensitive to the wings of the emission-line profiles, and thus a better indicator of outflows than the velocity dispersion (σ) from a Gaussian function. Usually W_{80} values larger than 600 km s^{-1} in the [O III]5007 Å line in powerful AGN are associated to outflows (e.g. Kakkad et al. 2020), while in low-luminosity AGN $W_{80} \gtrsim 500$ km s^{-1} have been attributed to ionized outflows (e.g. Wylezalek et al. 2020). We follow a similar procedure used in the optical by D'Agostino et al. (2019b)

to separate the contributions of star formation, shocks, and AGN ionization (see also D'Agostino et al. 2019a) and define an emission-line ratio function (f_{elr}) by

$$f_{elr} = \frac{\log X - \log X_{P02}}{\log X_{P98} - \log X_{P02}} \times \frac{\log Y - \log Y_{P02}}{\log Y_{P98} - \log Y_{P02}}, \quad (4)$$

with $X =$ H$_2$ 2.1218 µm/Brγ and $Y =$ [Fe II]1.2570 µm/Paβ, and P02 and P98 being the percentile 2 and 98 of the observed emission-line ratios, respectively. D'Agostino et al. (2019b) define the emission-line ratio function using [O III]5007/Hβ and [N II]6583/Hα line ratios in the optical and instead of use the P02 and P98 parameters, they use the minimum and maximum ratios. The P02 and P98 parameters are less sensitive to outliers than the minimum and maximum ratio values.

We present, in Fig. 11, the density plot of f_{elr} versus W_{80} (corrected for instrumental broadening) for all spaxels with H$_2$ 2.1218 µm/Brγ [Fe II]1.2570 µm/Paβ measurements from all galaxies. In green, we show the line ratios from the HLR region in the diagnostic diagram (Figs 2–7) and in red those from the AGN region. We do not show contours for the SF region as they are seen only in one galaxy. We find $W_{80[FeII]}$ larger than the typical limits above which they can be attributed to outflows. The $W_{80[FeII]}$ values derived in this work are larger than those obtained from the σ maps presented in Schönell et al. (2019) using the relation: $W80 = 2.563\sigma$ (Zakamska & Greene 2014). However, Schönell et al. (2019) fitted the emission lines by Gauss–Hermite series the relation above is no longer valid. In addition, the h_3 and h_4 maps from Schönell et al. (2019) present high values (with absolute values of up to 0.3), a clear indication that the line profiles are not Gaussian. A detailed discussion about the gas kinematics will be presented in a forthcoming paper (Bianchin et al., in preparation), but we find ionized outflows in all galaxies of our sample, based on the analysis of multi-Gaussian component fits to the near-IR emission lines. The interaction of these outflows with the interstellar medium can produce the shocks necessary to excite the H$_2$ and [Fe II] emission lines.

In Fig. 11, f_{elr} clearly separates two excitation regimes: the AGN regime, with $f_{elr} \leq 0.3$, and the HLR excitation regime for which f_{elr} is higher. In addition, in the HLR excitation regime, f_{elr} increases with $W_{80[FeII]}$, supporting the dominance of shock excitation. A similar increase of the emission-line ratio function with the gas velocity dispersion is seen in the optical and associated to shocks (D'Agostino et al. 2019a,b; Riffel et al. 2021). This suggests a strong contribution of shocks to the H$_2$ and [Fe II] emission from regions with high [Fe II]/Paβ and H$_2$/Brγ ratios in the galaxies of our sample.

Spaxels in the AGN region of the [Fe II]/Paβ versus H$_2$/Brγ diagram present a wide range in $W_{80[FeII]}$ and a smaller range of values of f_{elr}, as compared to the shock dominated spaxels. There is no trend between f_{elr} and $W_{80[FeII]}$ in the red contours of Fig. 11. This result indicates that shocks are less efficient in the production of line emission, when competing with the AGN radiation field, as found in the optical (Zakamska & Greene 2014). Thus, although a large fraction of the gas is outflowing and outflows naturally produce shocks, the AGN radiation field is the main responsible for the production of the H$_2$ and [Fe II] in the AGN region of the NIR diagnostic diagram. Some contribution of shocks in the AGN region of the diagnostic diagram is supported by the higher line ratios seen in the high-velocity range, as discussed above.

4.2.1 The origin of the H$_2$ emission

The near-IR H$_2$ emission lines in the AGN spectra originate from thermal processes (Fischer et al. 1987; Moorwood & Oliva 1990;

Veilleux, Goodrich & Hill 1997; Rodríguez-Ardila et al. 2005; Dors et al. 2012; Riffel et al. 2013a). The [Fe II]/Paβ versus H$_2$/Brγ diagnostic diagrams of all galaxies show that most of the line ratios are in the AGN and HLR regions. This indicates that thermal processes are the most relevant excitation mechanisms in our sample.

The H$_2$ vibrational and rotational temperatures are similar if the gas is in local thermal equilibrium (excited by thermal processes), while for fluorescent excitation, the rotational temperature is expected to be approximately 10 per cent of the vibrational temperature (Sternberg & Dalgarno 1989; Rodríguez-Ardila et al. 2004). We measure both $T_{\rm vib}$ and $T_{\rm rot}$ for NGC 788, NGC 3227 and NGC 5506 (see Fig. 9 and Table 2). For the these galaxies, the rotational temperatures are smaller than the vibrational, but larger than the values expected for fluorescent excitation. The largest difference is seen in NGC 788, for which the vibrational temperature is about twice the rotational temperature. For NGC 5506, the vibrational and rotational temperatures are the most similar, with $T_{\rm vib} \approx 1.4 T_{\rm rot}$ within the inner 100 pc of the galaxy and $T_{\rm vib} \approx T_{\rm rot}$ within the 0.5 arcsec. This indicates that thermal processes are dominant in all galaxies, but there is also some contribution from non-thermal processes, mainly in NGC 788.

The H$_2$ 2–1 S(1)/1–0 S(1) versus 1–0 S(2)/1–0 S(0) diagnostic diagrams (Fig. 8) confirm the conclusion that thermal processes dominate the H$_2$ emission in NGC 788, NGC 3227, and NGC 5506. Most of the points in the diagrams of Fig. 8 lie close to the range of values predicted by shock and X-ray excitation models, but some points are also seen close to region predicted for UV excitation of the H$_2$ in dense photon-dominated regions with cloud densities between 10^4 and 10^5 cm^{-3}, exposed to UV radiation field of of young 1–5 Myr star clusters (Davies et al. 2003, 2005).

We note the points from SF region of the [Fe II]1.2570 μm/Paβ versus H$_2$ 2.1218 μm/Brγ diagnostic diagram (Fig. 6) for NGC 5506 are seen distant from the region expected for non-thermal excitation and fall very close to the regions predicted by X-ray and shock models in the H$_2$ diagnostic diagram of Fig. 8. The H$_2$ and ionized gas emission-line flux distributions are seen almost perpendicular to each other, with the strongest emission in ionized gas being along the north–south direction, at the same locations classified as SF in the excitation map. The [O III]5007 Å is also more collimated along the north–south direction and its kinematics is consistent with a bipolar outflow (Fischer et al. 2013). This suggests the lower [Fe II]1.2570 μm/Paβ versus H$_2$ 2.1218 μm/Brγ line ratios along the north–south direction are not produced by star formation, but they may be a consequence of the AGN radiation field. The lower line ratios can be explained if the H$_2$ gas is partially dissociated by the AGN radiation or by shocks from the outflow, decreasing its abundance and consequently its emission, as found for other Seyfert galaxies (Storchi-Bergmann et al. 2009; Riffel et al. 2014a; Gnilka et al. 2020). Similarly, the [Fe II] abundance may be reduced by a strong radiation field, favouring higher excitation levels of the iron.

Although we were not able to measure the H$_2$ rotational temperatures and produce the H$_2$ 2–1 S(1)/1–0 S(1) versus 1–0 S(2)/1–0 S(0) excitation diagrams for Mrk 607, NGC 3516, and NGC 5899, the comparison of their [Fe II]1.2570 μm/Paβ versus H$_2$ 2.1218 μm/Brγ diagnostic diagram with those of the other galaxies is useful to understand how the H$_2$ emission originates in these objects. Mrk 607 and NGC 788 present very similar [Fe II]1.2570 μm/Paβ versus H$_2$ 2.1218 μm/Brγ diagrams, with all points in the AGN region, but overall small [Fe II]/Paβ. This, together with the fact that the emission of both ionized and molecular gas in Mrk 607 are similar and observed mainly along the major axis of the galaxy, suggest that we cannot rule out a contribution of fluorescent excitation to

the H$_2$ lines. NGC 3516 and NGC 5899 show high values of both [Fe II]1.2570 μm/Paβ and H$_2$ 2.1218 μm/Brγ, suggesting thermal processes are dominant in these galaxies.

4.2.2 The origin of the [Fe II] emission

The [Fe II] emission lines in AGN can be produced by photoionization and shocks. The photoionization models of Dors et al. (2012) and Riffel et al. (2013a) show that an increase in the [Fe II]/Paβ can originate from an enhancement of the Fe/O abundance. This suggests the correlation seen in Fig. 10 could originate in a combination of the amount of ionizing photons and a variation in the iron abundance. However, the [Fe II] emission can also be increased by shock excitation and indeed, the presence of shocks is supported by the high values of $W_{80[\rm FeII]}$ (Fig. 11).

The [Fe II] and [P II] have similar excitation temperatures and ionization potentials (16.2 and 19.8 eV, respectively) and the [Fe II]1.2570 μm/[P II]1.1886 μm can be used to investigate the origin of the [Fe II] emission. The iron is usually locked into dust grains and fast shocks can release it. In photoionized objects, such as the Orion Nebulae, [Fe II]1.2570 μm/[P II]1.1886 μm$\approx$2 and larger values indicate shocks have destroyed the dust grains, releasing the iron and increasing its abundance (Oliva et al. 2001; Jackson & Beswick 2007; Storchi-Bergmann et al. 2009; Riffel et al. 2010, 2020). In all galaxies, but NGC 788, most of the spaxels present [Fe II]1.2570 μm/[P II]1.1886 μm$>$2 indicating shocks play an important role in the production of the [Fe II] emission in our sample. In shock dominated objects, values of up to 20 are expected for this line ratio (e.g. Oliva et al. 2001). Such high values are observed only in some spaxels for NGC 5506, indicating the [Fe II] emission in the galaxies of our sample originates by a combination of photoionization and shocks. The comparison of the [Fe II]/[P II] versus [Fe II]/Paβ and H$_2$/Brγ versus [Fe II]/Paβ (Figs 2–7) shows that high values of H$_2$/Brγ and [Fe II]/Paβ are not a sufficient condition for shock excitation, although higher values of these ratios usually imply in larger [Fe II]/[P II] values (e.g. for NGC 3227 and NGC 5506). The shocks necessary to release the iron from the dust grains may be produced by the interaction of the outflows with the ambient gas, as indicated by the high $W_{80[\rm FeII]}$ values.

4.3 Coronal line emission

Coronal lines (CLs) are those produced by high ionization species, with ionization potentials typically larger than 100 eV. In the near-IR spectra of AGN, the most common CLs are [S VIII]0.9914 μm, [S IX]1.2523 μm, [Si X]1.4305 μm, [Si VI]1.9650 μm, [Al IX]2.0450 μm, [Ca VIII]2.3213 μm and [Si VII] 2.4830 μm (Rodríguez-Ardila et al. 2011). The high ionization gas in active galaxies can originate from photoionization due the AGN ionizing continuum (e.g. Shields & Oke 1975; Korista & Ferland 1989; Ferguson, Korista & Ferland 1997), shocks due to the interaction of a radio jet or outflows with the ambient gas (e.g. Osterbrock & Parker 1965; Rodríguez-Ardila & Fonseca-Faria 2020) or by a combination of photoionization and shocks (e.g. Viegas-Aldrovandi & Contini 1989; Contini & Viegas 2001). Photoionization seems to be the dominant excitation mechanism of CLs, but a contribution of shocks is necessary to reproduce the observed line intensities, especially at distances larger than $\sim$100 pc from the nucleus (Rodríguez-Ardila et al. (Rodríguez-Ardila et al. 2006, 2011; Geballe et al. 2009; Rodríguez-Ardila & Fonseca-Faria 2020).

Table 3. Extensions of the [S IX]1.2523 μm emission in our sample. FWHM$_{\rm SIX}$ is the full width at half-maximum of the [S IX]1.2523 μm flux distribution in arcseconds and parsecs, $R_{\rm SIX}$ is distance to the nucleus of the most extended [S IX] emission and FWHM$_{\rm PSF}$ is the *J*-band PSF (Riffel et al. 2018).

Galaxy	FWHM$_{\rm SIX}$ (arcsec)	FWHM$_{\rm SIX}$ (pc)	$R_{\rm SIX}$ (pc)	FWHM$_{\rm PSF}$ (arcsec)
NGC 788	0.32	90	185	0.13
Mrk 607	0.34	63	150	0.14
NGC 3227	0.36	30	80	0.13
NGC 3516	0.37	68	120	0.17
NGC 5506	0.47	60	100	0.15

The CLs usually trace highly ionized AGN-driven outflows, as indicated by their broader and blueshifted profiles as compared to those from lower ionization gas (Rodríguez-Ardila et al. 2002, 2006, 2017; Müller-Sánchez et al. 2011). For example, in the Circinus galaxy, highly ionized gas (traced by the [Fe VII]6087 μm) is seen up to 700 pc from the nucleus, and is tracing shock ionization due to the interaction of the radio jet with the ambient gas (Rodríguez-Ardila & Fonseca-Faria 2020).

Our NIFS data provides a unique capability to map the extension of the CL emission in nearby galaxies. The most prominent CL in in our observed spectral window is [S IX]1.2523 μm. The [S IX]1.2523 μm flux distribution is spatially resolved in all galaxies of our sample, except for NGC 5899, which only presents a very faint nuclear [S IX] emission. Table 3 lists the full width at half-maximum (FWHM$_{\rm SIX}$) of the [S IX] flux distributions and the most extended [S IX] emission at 3σ level detection ($R_{\rm SIX}$) for the galaxies of our sample. We find FWHM$_{\rm SIX}$ ranging from 30 to 90 pc, and $R_{\rm SIX}$ in the range 80–185 pc. The extension of the [S IX] in our sample is slightly larger than those found by Müller-Sánchez et al. (2011) using IFS of a sample of seven nearby Seyfert galaxies. They used the [Si VI]1.9650 μm emission as a tracer of the CL region and found FWHM from 8 to 60 pc and sizes from 8 to 150 pc. Prieto, Marco & Gallimore (2005) derived extensions of the [Si VII]2.48 μm from 30 to 200 pc using adaptive optics narrow band images with the ESO/VLT. At these scales, a pure photoionization scenario fails to reproduce the CLs intensities, favouring an additional contribution of shocks to the coronal emission (e.g. Rodríguez-Ardila et al. 2006; Mazzalay et al. 2013; Rodríguez-Ardila & Fonseca-Faria 2020). Most of galaxies of our sample show compact radio emission (Nagar et al. 1999; Schmitt et al. 2001). The only exception is NGC 3227, which shows extended radio emission along PA $\approx -10°$ (Mundell et al. 1995). However, the CL emission in this galaxy does not present a clear extension along the direction of the radio structure. On the other hand, ionized outflows are common in our sample (Bianchin et al., in preparation) and thus, the most likely scenario to produce CLs observed in our sample is the combination of photoionization and shocks due to AGN-driven outflows (e.g. Viegas-Aldrovandi & Contini 1989; Contini & Viegas 2001).

5 CONCLUSIONS

We use Gemini NIFS *J*- and *K*-band data to investigate the origin of the near-IR emission lines in the inner few hundred pc of six luminous Seyfert galaxies (NGC 788, Mrk 607, NGC 3227, NGC 3516, NGC 5506, and NGC 5899) at spatial resolutions of 10 to 40 pc. Our main conclusions are the following:

(i) For all galaxies, the [Fe II]1.2570 μm/Paβ versus H$_2$ 2.1218 μm/Brγ diagrams present values in the AGN and HLR regions at most locations. We find a strong correlation between [Fe II]1.2570 μm/Paβ and H$_2$ 2.1218 μm/Brγ represented by the linear equation $\log([\mathrm{Fe\,II}]/\mathrm{Pa}\beta) = (0.65 \pm 0.026) \times \log(\mathrm{H}_2/\mathrm{Br}\gamma) - (0.12 \pm 0.013)$ which is consistent with the previous result of Riffel et al. (2013a), possibly indicating a common excitation origin.

(ii) The HLR regions in the [Fe II]1.2570 μm/Paβ versus H$_2$ 2.1218 μm/Brγ diagnostic diagram are observed surrounding the AGN region, with no preferential orientation relative to the orientation of the ionization structure.

(iii) We define an emission-line ratio function ($f_{\rm elr}$) that depends on the [Fe II]1.2570 μm/Paβ versus H$_2$ 2.1218 μm/Brγ line ratios and presents values in the range $\sim$0–1. We find a correlation between this function and $W_{80[\mathrm{FeII}]}$, where $f_{\rm elr}$ increases with $W_{80[\mathrm{FeII}]}$ for the HLR regions of the galaxies indicating shocks produced by gas outflows contribute to the line emission in locations with high [Fe II]1.2570 μm/Paβ and H$_2$ 2.1218 μm/Brγ values.

(iv) The H$_2$ emission lines are excited by thermal processes in all galaxies. Based on line-ratio diagnostic diagrams and the trend seen between $f_{\rm elr}$ and the $W_{80[\mathrm{FeII}]}$, our results indicate, for spaxels in the HLR region, the main process exciting the H$_2$ lines are shocks produced by AGN-driven winds. While for spaxels in the AGN region of the diagnostic diagram, the AGN radiation field is responsible for the observed H$_2$ emission. A small contribution of shocks cannot be ruled out in the AGN region, as indicated by the higher line ratios obtained by computing the line fluxes at velocities of $|v| > 100\,\mathrm{km\,s}^{-1}$, compared to those using $|v| < 100\,\mathrm{km\,s}^{-1}$, relative to the peak velocity.

(v) The [Fe II] emission in our sample originates from a combination of photoionization by the central source and shocks due to AGN winds, as indicated by the [Fe II]1.2570 μm/[P II]1.1886 μm high values (2–20), line ratios and the correlation between $f_{\rm elr}$ and the $W_{80[\mathrm{FeII}]}$ for the HLR region.

(vi) The CL region, traced by [S IX]1.2523 μm emission, extends out between 80 and 185 pc from the galaxy nucleus in five galaxies and is likely produced by AGN photoionization. The [S IX]1.2523 μm emission line is only detected in NGC 5899 using an integrated spectrum.

DATA AVAILABILITY

The data used in this work are publicly available online via the GEMINI archive https://archive.gemini.edu/searchform, under the following program codes: GN-2012B-Q-45, GN-2013A-Q-48, GN-2015A-Q-3, GN-2015B-Q-29, and GN-2016A-Q-6. The processed datacubes used in this paper will be shared on reasonable request to the corresponding author.

REFERENCES

Ann H. B., Seo M., Ha D. K., 2015, ApJS, 217, 27
Arribas S., Mediavilla E., 1994, ApJ, 437, 149
Black J. H., van Dishoeck E. F., 1987, ApJ, 322, 412
Blanco P. R., Ward M. J., Wright G. S., 1990, MNRAS, 242, 4P
Colbert E. J. M., Baum S. A., Gallimore J. F., O'Dea C. P., Christensen J. A., 1996, ApJ, 467, 551
Colina L. et al., 2015, A&A, 578, A48
Contini M., Viegas S. M., 2001, ApJS, 132, 211
D'Agostino J. J., Kewley L. J., Groves B. A., Medling A., Dopita M. A., Thomas A. D., 2019a, MNRAS, 485, L38
D'Agostino J. J. et al., 2019b, MNRAS, 487, 4153
Dale D. A. et al., 2004, ApJ, 601, 813
Davies R. I., Sternberg A., Lehnert M., Tacconi-Garman L. E., 2003, ApJ, 597, 907
Davies R. I., Sternberg A., Lehnert M. D., Tacconi-Garman L. E., 2005, ApJ, 633, 105
Davies R. I. et al., 2014, ApJ, 792, 101
de Vaucouleurs G., de Vaucouleurs A., Corwin, Herold G. J., Buta R. J., Paturel G., Fouque P., 1991, Third Reference Catalogue of Bright Galaxies. Springer-Verlag, New York
Dors O. L., Jr, Riffel R. A., Cardaci M. V., Hägele G. F., Krabbe A. C., Pérez-Montero E., Rodrigues I., 2012, MNRAS, 422, 252
Draine B. T., Woods D. T., 1990, ApJ, 363, 464
Durré M., Mould J., 2018, ApJ, 867, 149
Ferguson J. W., Korista K. T., Ferland G. J., 1997, ApJS, 110, 287
Ferruit P., Wilson A. S., Mulchaey J., 2000, ApJS, 128, 139
Fischer J., Geballe T. R., Smith H. A., Simon M., Storey J. W. V., 1987, ApJ, 320, 667
Fischer T. C., Crenshaw D. M., Kraemer S. B., Schmitt H. R., 2013, ApJS, 209, 1
Forbes D. A., Ward M. J., 1993, ApJ, 416, 150
Freitas I. C. et al., 2018, MNRAS, 476, 2760

Geballe T. R., Mason R. E., Rodríguez-Ardila A., Axon D. J., 2009, ApJ, 701, 1710
Glidden A., Rose M., Elvis M., McDowell J., 2016, ApJ, 824, 34
Gnilka C. L. et al., 2020, ApJ, 893, 80
Goad J. W., Gallagher J. S. I., 1987, AJ, 94, 640
Guillard P., Boulanger F., Pineau Des Forêts G., Appleton P. N., 2009, A&A, 502, 515
Ho L. C., Filippenko A. V., Sargent W. L. W., 1997, ApJS, 112, 315
Ho I. T. et al., 2014, MNRAS, 444, 3894
Hollenbach D., McKee C. F., 1989, ApJ, 342, 306
Ichikawa K., Ricci C., Ueda Y., Matsuoka K., Toba Y., Kawamuro T., Trakhtenbrot B., Koss M. J., 2017, ApJ, 835, 74
Ilić D. et al., 2020, A&A, 638, A13
Izotov Y. I., Thuan T. X., 2011, ApJ, 734, 82
Jackson N., Beswick R. J., 2007, MNRAS, 376, 719
Kakkad D. et al., 2020, A&A, 642, 32
Kewley L. J., Heisler C. A., Dopita M. A., Lumsden S., 2001, ApJS, 132, 37
Knop R. A., Armus L., Matthews K., Murphy T. W., Soifer B. T., 2001, AJ, 122, 764
Korista K. T., Ferland G. J., 1989, ApJ, 343, 678
Kwan J. H., Gatley I., Merrill K. M., Probst R., Weintraub D. A., 1977, ApJ, 216, 713
Lamperti I. et al., 2017, MNRAS, 467, 540
Larkin J. E., Armus L., Knop R. A., Soifer B. T., Matthews K., 1998, ApJS, 114, 59
Lepp S., McCray R., 1983, ApJ, 269, 560
Liu G., Zakamska N. L., Greene J. E., Nesvadba N. P. H., Liu X., 2013, MNRAS, 436, 2576
McGregor P. J. et al., 2003, Proc. SPIE Conf. Ser. Gemini Near-Infrared Integral Field Spectrograph (NIFS). SPIE, Bellingham, p. 1581
Maiolino R., Stanga R., Salvati M., Rodriguez Espinosa J. M., 1994, A&A, 290, 40
Maloney P. R., Hollenbach D. J., Tielens A. G. G. M., 1996, ApJ, 466, 561
May D., Steiner J. E., 2017, MNRAS, 469, 994
May D., Rodríguez-Ardila A., Prieto M. A., Fernández-Ontiveros J. A., Diaz Y., Mazzalay X., 2018, MNRAS, 481, L105
May D., Steiner J. E., Menezes R. B., Williams D. R. A., Wang J., 2020, MNRAS, 496, 1488
Mazzalay X., Rodríguez-Ardila A., Komossa S., McGregor P. J., 2013, MNRAS, 430, 2411
Moorwood A. F. M., Oliva E., 1990, A&A, 239, 78
Mouri H., 1994, ApJ, 427, 777
Mouri H., Nishida M., Taniguchi Y., Kawara K., 1990, ApJ, 360, 55
Mouri H., Kawara K., Taniguchi Y., 1993, ApJ, 406, 52
Müller-Sánchez F., Prieto M. A., Hicks E. K. S., Vives-Arias H., Davies R. I., Malkan M., Tacconi L. J., Genzel R., 2011, ApJ, 739, 69
Mundell C. G., Holloway A. J., Pedlar A., Meaburn J., Kukula M. J., Axon D. J., 1995, MNRAS, 275, 67
Nagar N. M., Wilson A. S., Mulchaey J. S., Gallimore J. F., 1999, ApJS, 120, 209
Oh K. et al., 2018, ApJS, 235, 4
Oliva E. et al., 2001, A&A, 369, L5
Osterbrock D. E., Parker R. A. R., 1965, ApJ, 141, 892
Prieto M. A., Marco O., Gallimore J., 2005, MNRAS, 364, L28
Reunanen J., Kotilainen J. K., Prieto M. A., 2002, MNRAS, 331, 154
Riffel R. A., 2010, Ap&SS, 327, 239
Riffel R. A., Storchi-Bergmann T., 2011a, MNRAS, 411, 469
Riffel R. A., Storchi-Bergmann T., 2011b, MNRAS, 417, 2752
Riffel R. A., Storchi-Bergmann T., Winge C., Barbosa F. K. B., 2006a, MNRAS, 373, 2
Riffel R., Rodríguez-Ardila A., Pastoriza M. G., 2006b, A&A, 457, 61
Riffel R. A., Storchi-Bergmann T., Winge C., McGregor P. J., Beck T., Schmitt H., 2008, MNRAS, 385, 1129
Riffel R. A., Storchi-Bergmann T., Nagar N. M., 2010, MNRAS, 404, 166
Riffel R., Rodríguez-Ardila A., Aleman I., Brotherton M. S., Pastoriza M. G., Bonatto C., Dors O. L., 2013a, MNRAS, 430, 2002
Riffel R. A., Storchi-Bergmann T., Winge C., 2013b, MNRAS, 430, 2249

Riffel R. A., Vale T. B., Storchi-Bergmann T., McGregor P. J., 2014a, MNRAS, 442, 656

Riffel R. A., Storchi-Bergmann T., Riffel R., 2014b, ApJ, 780, L24

Riffel R. A., Storchi-Bergmann T., Riffel R., 2015, MNRAS, 451, 3587

Riffel R. A., Storchi-Bergmann T., Riffel R., Dahmer-Hahn L. G., Diniz M. R., Schönell A. J., Dametto N. Z., 2017, MNRAS, 470, 992

Riffel R. A. et al., 2018, MNRAS, 474, 1373

Riffel R. et al., 2019, MNRAS, 486, 3228

Riffel R. A., Storchi-Bergmann T., Zakamska N. L., Riffel R., 2020, MNRAS, 496, 4857

Riffel R. A. et al., 2021, MNRAS, 501, L54

Rodríguez-Ardila A., Fonseca-Faria M. A., 2020, ApJ, 895, L9

Rodríguez-Ardila A., Viegas S. M., Pastoriza M. G., Prato L., 2002, ApJ, 579, 214

Rodríguez-Ardila A., Pastoriza M. G., Viegas S., Sigut T. A. A., Pradhan A. K., 2004, A&A, 425, 457

Rodríguez-Ardila A., Riffel R., Pastoriza M. G., 2005, MNRAS, 364, 1041

Rodríguez-Ardila A., Prieto M. A., Viegas S., Gruenwald R., 2006, ApJ, 653, 1098

Rodríguez-Ardila A., Prieto M. A., Portilla J. G., Tejeiro J. M., 2011, ApJ, 743, 100

Rodríguez-Ardila A., Prieto M. A., Mazzalay X., Fernández-Ontiveros J. A., Luque R., Müller-Sánchez F., 2017, MNRAS, 470, 2845

Ruschel-Dutra D., 2020, danielrd6/ifscube v1.0. Zenodo. Available at: https://doi.org/10.5281/zenodo.3945237

Schinnerer E., Eckart A., Tacconi L. J., 2000, ApJ, 533, 826

Schmitt H. R., Ulvestad J. S., Antonucci R. R. J., Kinney A. L., 2001, ApJS, 132, 199

Schmitt H. R., Donley J. L., Antonucci R. R. J., Hutchings J. B., Kinney A. L., 2003, ApJS, 148, 327

Schönell A. J., Storchi-Bergmann T., Riffel R. A., Riffel R., Bianchin M., Dahmer-Hahn L. G., Diniz M. R., Dametto N. Z., 2019, MNRAS, 485, 2054

Shields G. A., Oke J. B., 1975, ApJ, 197, 5

Simpson C., Forbes D. A., Baker A. C., Ward M. J., 1996, MNRAS, 283, 777

Smith M. D., 1995, A&A, 296, 789

Sternberg A., Dalgarno A., 1989, ApJ, 338, 197

Storchi-Bergmann T., McGregor P. J., Riffel R. A., Simões Lopes R., Beck T., Dopita M., 2009, MNRAS, 394, 1148

Storchi-Bergmann T., Lopes R. D. S., McGregor P. J., Riffel R. A., Beck T., Martini P., 2010, MNRAS, 402, 819

Turner J., Kirby-Docken K., Dalgarno A., 1977, ApJS, 35, 281

Veilleux S., Tully R. B., Bland-Hawthorn J., 1993, AJ, 105, 1318

Veilleux S., Goodrich R. W., Hill G. J., 1997, ApJ, 477, 631

Véron-Cetty M. P., Véron P., 2006, A&A, 455, 773

Viegas-Aldrovandi S. M., Contini M., 1989, A&A, 215, 253

Wylezalek D. et al., 2017, MNRAS, 467, 2612

Wylezalek D., Flores A. M., Zakamska N. L., Greene J. E., Riffel R. A., 2020, MNRAS, 492, 4680

Zakamska N. L., Greene J. E., 2014, MNRAS, 442, 784

This paper has been typeset from a TeX/LaTeX file prepared by the author.